Published in final edited form as:
J Magn Reson Imaging. 2013 September ; 38(3): 511–529. doi:10.1002/jmri.24168.

Biomedical Applications of Sodium MRI *In Vivo*

Guillaume Madelin, PhD* and **Ravinder R. Regatte, PhD**
New York University Langone Medical Center, Department of Radiology, Center for Biomedical Imaging, New York, NY 10016, USA

Abstract

In this article, we present an up-to-date overview of the potential biomedical applications of sodium MRI *in vivo*. Sodium MRI is a subject of increasing interest in translational imaging research as it can give some direct and quantitative biochemical information on the tissue viability, cell integrity and function, and therefore not only help the diagnosis but also the prognosis of diseases and treatment outcomes. It has already been applied *in vivo* in most of human tissues, such as brain for stroke or tumor detection and therapeutic response, in breast cancer, in articular cartilage, in muscle and in kidney, and it was shown in some studies that it could provide very useful new information not available through standard proton MRI. However, this technique is still very challenging due to the low detectable sodium signal in biological tissue with MRI and hardware/software limitations of the clinical scanners. The article is divided in three parts: (1) the role of sodium in biological tissues, (2) a short review on sodium magnetic resonance, and (3) a review of some studies on sodium MRI on different organs/diseases to date.

Keywords

Sodium; magnetic resonance imaging; biochemical; quadrupolar

INTRODUCTION

Proton magnetic resonance imaging (MRI) can generate more than 30 different kinds of image contrast (and still counting) which can give the physicians crucial information on the anatomy, and sometimes function, of the organs under investigation. Most of the known diseases can be studied with this imaging technique in order to assess their presence and/or degree of possible harm to the body. However, the information from standard MRI cannot provide direct biochemical information about the tissue viability (homeostasis, cell membrane integrity), or predict possible outcomes from different treatments. Sodium MRI could provide some of this complementary information in a quantitative and non-invasive manner.

Sodium, symbol ^{23}Na, is a quadrupolar nucleus with spin 3/2 which yields the second strongest nuclear magnetic resonance (NMR) signal among all nuclei present in biological tissues, after proton ^{1}H. The NMR sensitivity for sodium is 9.2% of the proton sensitivity and the concentration *in vivo* is a few thousand times lower than the proton concentration. As a consequence, sodium MRI has an average signal-to-noise (SNR) ratio which is around 3000 to 20000 times lower than the SNR of proton MRI SNR (depending on organs). Due to the increase of available magnetic fields for MRI scanners (1.5T, 3T, 7T, 9.4T), hardware capabilities such as high gradient strengths with high slew rates, and new double-tuned

*Corresponding Author: New York University Langone Medical Center, Department of Radiology, Center for Biomedical Imaging, 660 First Avenue, 4th Floor, New York, NY 10016, USA. Telephone: 1-212-263-3343. Fax: 1-212-263-7541. guillaume.madelin@nyumc.org.

radiofrequency (RF) coils, sodium MRI is now possible in a reasonable time (around 10 to 15 minutes) with a resolution of a few millimeters, and has already been tested *in vivo* in many human organs such as human brain, cartilage, kidneys, heart, muscle, or breast, that will be described in this review article. Sodium MRI is still a subject of investigation for assessing its medical utility as a complement to proton MRI or other imaging modalities such as PET and CT, and determining the new functional/biochemical information that it can provide.

The goal of this review is to describe the potential biomedical applications of sodium MRI *in vivo* and is divided in three parts: (1) the role of sodium in biological tissues, (2) a short review on sodium magnetic resonance, and (3) a review of some studies on sodium MRI on different organs/diseases to date.

SODIUM IN BIOLOGICAL TISSUES

Sodium is a vital component of the human body. It is an important electrolyte that helps maintain the homeostasis of the organism through osmoregulation (maintain blood and body fluid volume) and pH regulation (1). It is also involved in the cell physiology through the transmembrane electrochemical gradient, in heart activity, in the transmission of nerve impulses and muscle contractions through propagation of action potential in neurons and muscle cells via the sodium channels. The intracellular volume fraction is generally of the order of 80% of the tissues with a sodium concentration of 10–15 mM (or mmol/L), and the extracellular volume fraction (including the vascular compartment) is around 20%, with a sodium concentration of 140–150 mM. Cells in healthy tissues maintain this large sodium concentration gradient between the intracellular and extracellular compartments across the cell membrane, and any impairment of energy metabolism or insult to the cell membrane integrity leads to an increase of intracellular sodium concentration. Sodium concentrations are therefore very sensitive to changes in the metabolic state of tissues and integrity of cell membranes. The sodium influx and outflux in cells can occur by several routes such as Na^+ channels, Na^+/Ca^+ exchange (NCX), Na^+/H^+ exchange (NHE), Na^+/HCO_{3-} co-transporter, $Na^+/K^+/2Cl^-$ co-transporter, Na^+/Mg^+ exchange and most importantly through the Na^+/K^+-ATPase (2).

The Na^+/K^+-ATPase (also called sodium-potassium pump, or just sodium pump) is present within the membrane of every animal cell (3, 4). It is a plasma membrane-associated protein complex that is expressed in most eukaryotic cells and can be considered either as an enzyme (ATPase) or as an ion transporter (the sodium pump). Its main function is to maintain the sodium and potassium gradients across the membrane by pumping three intracellular sodium ions out of the cell and two extracellular potassium ions within the cell (see Fig. 1). This ion transport is performed against the electrochemical Na^+ and K^+ gradients existing across the cell membrane and therefore requires energy provided by adenosine triphosphate (ATP) hydrolysis. This high electrochemical sodium (and potassium) gradient is essential to protect the cell from bursting as a result of osmotic swelling, it regulates the cell volume, and it helps maintain the resting cell membrane potential which can be used for transmitting nerve impulses (Na^+ and K^+ have to be actively pumped back after an excitation event of a nerve or muscle membrane potential), and for pumping ions (protons, calcium, chloride, phosphate), metabolites (glucose, amino acids) or neurotransmitters (glutamate) across the cell membrane. Regulation of Na^+/K^+-ATPase therefore plays a key role in the etiology of some pathological processes. When the demand for ATP exceeds its production (when cell membrane leaks overwhelm the pumping capacity), the ATP supply for the Na^+/K^+-ATPase will be insufficient to maintain the electrochemical sodium and thus an increase of intracellular sodium concentration can be

observed, leading to swelling due to changes in osmolarity and eventually leading to cell death.

SODIUM MAGNETIC RESONANCE

Short History of Sodium MR

The bar chart in Fig. 2 present the distribution of publications on sodium NMR and/or MRI over the years since the discovery of magnetic resonance (5, 6). We can notice a peak of publications in the period 1991–1995 for the combination of sodium NMR (spectroscopy) and MRI, then a decrease in total publications while the number of sodium MRI publications alone continues to increase since the early 1980s. A shift of interest appears from sodium NMR spectroscopy to MRI, which is probably due to the increasing availability of scanners with increasing fields and therefore the possibility to perform new research with sodium MRI *in vivo*. Biological tissues were already investigated with sodium NMR spectroscopy in the early 1970s (7, 8) and with sodium MRI in the early 1980s (9–11), first on animals and then on human brain (12) and human heart and abdomen (13). Sodium MRI was thereafter applied for brain tumor and ischemia detection in the late 1980s (14). The years 1990s saw an increase of interest in sodium MRI, due to the increase of the magnetic fields (≥1.5T), improvements of electronics and RF coils, and new rapid pulse sequences that allow sodium image acquisitions within a few minutes with a reasonable resolution of a few millimeters (15), or new contrasts such as triple quantum filtered images (16–18). This trend continued in the 2000s until today.

Sodium NMR Properties

The sodium nucleus has a spin I = 3/2 and possesses a quadrupolar moment Q which interacts with the electric field gradients (EFG) generated by the electronic configuration of the molecular environment surrounding the nucleus. Its gyromagnetic ratio γ_{Na} = 70.808493×10^6 radT^{-1}s^{-1} corresponds to 26% of the proton γ_p. In general, sodium in solids experience quadrupolar interactions, while in liquids the static quadrupolar interaction is averaged to zero. In the intermediate regimes, e.g. in biological tissues, the quadrupolar interaction results in a biexponential transverse relaxation behavior ($T2_{short}$ of the order 0.5–5 ms and $T2_{long}$ of the order 15–30 ms). The dominance of quadrupolar relaxation mechanism for NMR signals can allow a sensitive characterization of the molecular environment of the sodium ions. It is difficult to obtain reliable information about the biexponential relaxation from conventional simple single-pulse/single quantum (SQ) NMR experiments. It has been shown that in the presence of biexponential relaxation, multiple quantum coherences (MQC) can be created and detected with multiple quantum filtered (MQF) sequences (19), and thus give more information about the interaction of sodium ions with their environment. Some ranges of values for sodium concentrations and relaxation times in biological tissues are presented in Table 1, and are just given as an indicator of the order of values that we can encounter *in vivo*. The dependence of relaxation the times *in vivo* with the magnetic field is still not well documented, and depends strongly on the motional regime in which the sodium nuclei are present (see the “Sodium NMR Spectra” section).

Spherical Tensor Operator

A convenient way to describe the various processes occurring to the different sodium spin components during a RF pulse sequence is by using the irreducible spherical tensor operator (ISTO) basis, T_{lp}, where l is the rank and p is the order (or coherence) of the tensor (20–22). These tensors are composed of combinations of the more familiar spin operators I_z and $I_\pm$ = $I_x \pm iI_y$. The irreducible tensor operators used to describe the density operator and the Hamiltonians for a spin 3/2 are given in Table 2. In order to follow the sequence of events at

high magnetic fields, one should observe two simple rules: (1) a non-selective RF pulse can change the coherence p within the limits of $|p| \leq l$, while keeping l constant; (2) relaxation and quadrupolar, dipolar or J-coupling interactions can change the rank l, while keeping p constant. The ISTO are a very useful tool for describing and designing pulse sequences in order to select the coherences of interest for imaging (single, double and triple quantum coherences -SQC, DQC and TQC), which originate from different motional regimes and degrees of order in the tissues under investigation. The SQCs $T_{1\pm1}$, corresponding to transverse magnetization, are the only coherences detectable with the conventional NMR apparatus, but they can be generated from different pathways involving DQCs and TQCs with appropriate phase cycling (an example is given in the "Multiple Quantum Filter" section and in Fig. 5).

Sodium NMR Spectra

Depending on the motional regime of the system, the energy levels of the system and the relaxation rates can be modified, giving one or many NMR peaks in the SQ ^{23}Na spectra, as shown on Fig. 3. Three motional regimes and four different types of spectra are possible, depending on the nature of the spin dynamics and the nature of the molecular environment (23–26). In this section, we consider the following approximations: the Na^+ ions are present in a single compartment with a single rotational correlation time τ_c, they precess at the Larmor angular frequency ω_0, and they can be subject to an anisotropic residual quadrupolar interaction (RQI) ω_Q.

Isotropic motion with motional narrowing ($\omega_0\tau_c \ll 1$)—In a system of isotropic rapid motion such as a fluid, all orientations of the EFG are equally probable, the quadrupolar interaction is averaged to zero on the time scale of the inverse of the Larmor frequency, and the four energy levels are equally distant by the angular frequency ω_0. The ^{23}Na spectrum is then composed of a single resonance line at ω_0, as shown in the type-d spectrum in Fig. 3. Both transverse and longitudinal relaxations are simple exponential decays.

Isotropic motion without motional narrowing ($\omega_0\tau_c \approx 1$)—In tissues where the macromolecular motion associated with the nucleus is isotropic but of the same order of the Larmor frequency, the quadrupolar interaction dominates the relaxation. The satellite and central transitions have different transverse relaxation rates and can be dynamically shifted from the Larmor frequency. However, these shifts are much smaller than the linewidths and very difficult to detect. This situation can correspond to a biological-like type-c spectrum in Fig. 3. It is a 'biexponential' ('super-Lorentzian') spectrum, in which the satellite peaks have coalesced into a single broad homogeneous peak. In this case, even in the absence of any quadrupolar splitting, biexponential relaxation can create MQC which can be detected by triple quantum filtering (TQF).

Anisotropic motion without motional narrowing ($\omega_0\tau_c > 1$)—In this case, the sodium nuclei interact with ordered structures in their environment. The nuclei experiment non-averaged EFGs and therefore a residual quadrupolar interaction ω_Q that can induce a shift in energy levels of the spin system and create multiple lines in the spectrum.

1. If ω_Q is small compared to the relaxation dynamics of the spins, the relaxation rates are real and there is no line splitting despite the presence of RQI. The SQ spectrum is a sum of three Lorentzians and the RQI influences the linewidths and amplitudes of the components. This case can be still described by a type-c spectrum in Fig. 3, and here the double quantum filter (DQF) signal due to even rank coherence $T_{2\pm2}$ can be used to detect and measure ω_Q.

2. If ω_Q is high compared to the relaxation dynamics of the spins, the relaxation times corresponding to the outer transitions are complex and the satellite transitions are shifted from the central line. This case corresponds to a powder-like type-b spectrum in Fig. 3. The DQF signal from $T_{2\pm2}$ can also be used to measure ω_Q.
3. If ω_Q is much higher than the relaxation dynamics of the spins, the energy levels are all shifted by the RQI, resulting in three distinct peaks in the spectrum. The central transition and the two satellite transitions are separated by ω_Q. This frequency separation between the lines provides therefore indirect information about RQI and the magnitude of ordering in the system. This case can be described by a crystal-like type-a spectrum in Fig. 3.

Spectra in biological tissues—Sodium spectra are mostly of type d in fluid biological tissues (synovial fluid, cerebrospinal fluid), and of type c in other tissues, depending on their viscosity and degree of order (brain white matter, muscle and cartilage could even have some local degree of anisotropy leading to a type b spectrum very locally). Type-a spectra are very unlikely to be found *in vivo* as they are obtained from very ordered systems such as solids and liquid crystals. In biological tissues, the correlation times τ_c are generally in the range from picoseconds (fluids) to nanoseconds (more viscous tissues) (23, 25). The spectra shapes also depend on the magnetic field at which they are acquired, as ω_0 increases with the field, and therefore the motional narrowing approximation can shift spectra from type c to b. The consequences of the spectra shapes on imaging are possible loss of signal due to long TE (miss the broad component of signal with short T2) or selective RF transmit bandwidth, or signal leakage from one pixel to another one due to limited acquisition bandwidth.

MRI Pulse Sequences

Due to the short (biexponential) T2 relaxation of sodium in vivo, ultrashort TE (UTE) sequences are recommended to acquire the images. The first sodium images were acquired with 3D gradient echo sequences where the TE was minimized by using non-selective hard pulse (27). TE of the order of 2–4 ms can be obtained with this method. Shorter TEs (< 1ms) can generally be obtained by acquiring the data from the center of the k-space in a radial or spiral fashion. The most common type of this kind of sequence is the 3D radial sequence which has been used widely for sodium MRI (28). This method can then be improved from the signal-to-noise ratio (SNR) and time efficiency point of view by modifying the density of acquisition points along the projections and also by twisting the radial projection in the outer k-space in an optimal manner in order to fill the k-space more homogeneously and improve the point spread function of the acquisition method. This is done in sequences such as density adapted radial sequence (29), twisted projection imaging (TPI) and its variations (15, 30, 31), 3D cones (32) or FLORET (33). Examples of k-space trajectories from 3D radial and TPI sequences are shown in Fig. 4. These two sequences are now the standard for sodium MRI. Other UTE sequences, such as SPRITE (34, 35), SWIFT (36), ZTE (37), PETRA (38) have also been developed with even shorter TEs, but are still under investigation about their application to *in vivo* sodium MRI. Data acquired with all these non-Cartesian sequences are generally reconstructed using regridding (39–41) or non-uniform fast Fourier transform (NUFFT) algorithms (42, 43).

Multiple Quantum Filters (MQF)

In order to detect MQC from different types of spectrum and therefore obtain some information about the biological environment of the sodium nuclei, MQF can be implemented before the NMR acquisitions (44–46). MQF are described in Fig. 5. A first pulse of angle θ_1 is applied to the system to flip the longitudinal magnetization T_{10} into the

transverse plane, creating a transverse magnetization $T_{1\pm1}$. During the preparation time τ, the transverse magnetization $T_{1\pm1}$ evolves in the presence of relaxation and RQI, creating single quantum coherences (SQC) with different rank ($T_{1\pm1}$, $T_{2\pm1}$, $T_{3\pm1}$). In isotropic liquids only odd rank tensors $T_{3\pm1}$ can be formed during τ under the influence of quadrupolar relaxation. In anisotropic media, where the RQI does not average to zero, even rank tensors $T_{2\pm1}$ can be also formed. A second pulse θ_2 converts these SQC into double and triple quantum coherences $T_{2\pm2}$, $T_{3\pm2}$ (DQC), $T_{3\pm3}$ (TQC). During the evolution time δ, the MQCs evolve with their characteristic relaxation times, and generally, δ is kept very short to avoid their decay. Since the MQCs cannot be detected directly, the final RF pulse θ_3 converts the MQCs into SQCs $T_{2\pm1}$, $T_{3\pm1}$ which then evolve under relaxation and RQI into the detectable SQC $T_{1\pm1}$ during the acquisition time t_{acq}. A 180° RF pulse can also be applied in the middle of the preparation time τ in order to refocus the chemical shifts and magnetic field inhomogeneities. However, as MQF are very sensitive to RF imperfections, and it has been shown that filters without this refocusing pulse generate a higher signal and are more robust to RF inhomogeneities for MQF imaging (47). The formation of DQC and TQC is detected separately by choosing the appropriate RF pulse flip angles and phase cycling (see Fig. 4). DQF can detect the contribution of two tensors, $T_{2\pm1}$ and $T_{3\pm1}$, due to the slow motion regime and RQI in anisotropic media. if $\theta_1 = \theta_2 = \theta_3 = 90°$, contributions from both $T_{2\pm1}$ and $T_{3\pm1}$ can be detected. If $\theta_1 = 90°$ and $\theta_2 = \theta_3 = 54.7°$ (magic angle), only the contribution of $T_{2\pm1}$ is detected, which arises only from the anisotropic RQI. Only $T_{3\pm1}$ due to the slow motion regime can be detected by the TQF sequence.

Extracellular/Fluid Sodium Suppression

In many diseases, a sodium concentration increase is detected, which can be caused by either an increase of intracellular sodium concentration, increase of extracellular volume with a constant concentration (140 mM) or increase of vascularization. It is widely believed that the most sensitive way to study the viability of tissues *in vivo* with sodium MRI should be done by isolating the sodium signal from the intracellular compartment, as intracellular sodium concentration and/or relaxation properties should give more useful information on the cells integrity (48). Four techniques have been suggested to suppress extracellular sodium and/or the signal from fluids around of the tissue of interest:

Shift Reagents (SR)—This technique is based on the use a ^{23}Na chemical shift reagent based on lanthanide chelates as $Tm(DOTP)^{5-}$ or $Dy(TTHA)^{3-}$ (49–51). These compounds do not penetrate the cell membrane and therefore create a frequency offset for the sodium nuclei in the extracellular space. However, they don't cross the blood-brain barrier, and because of their moderate toxicity, these SR can't be used in humans.

Diffusion—Diffusion-based techniques can separate the sodium signal from the intracellular and extracellular compartments based on the differences between the motional properties of the ions in these compartments (52). However, the fast T2 relaxation of sodium and its low gyromagnetic ratio require the use of very large magnetic field gradients, which can cannot to be effectively implemented in clinical MRI scanners.

Inversion Recovery (IR)—The IR technique is based on the difference in the T1 relaxation of the sodium nuclei in different compartments. As the T1 relaxation time of the extracellular sodium or in fluid can be significantly longer than the T1 of the intracellular sodium, IR can be used to eliminate the signal contribution from either environment (53–55).

MQF—The MQF technique is based on the different T2 relaxation properties of the sodium nuclei in different compartments. Depending on the pulse amplitudes and the phase cycling,

the TQF and DQF filters can allow the signal coming from the sodium DQC or TQC to be read by the acquisition sequence. However, the signal following a MQF sequence is a small fraction of the maximum SQ signal (around 10% has been given as a typical value *in vivo*). Several reports estimate that the MQF NMR signal in biological tissues comes primarily from the intracellular sodium (56–59), but this statement is still controversial (48, 60, 61).

IR and the MQF are the two only techniques that can be currently applied in sodium MRI *in vivo*. Despite the fact that they cannot really completely separate the different compartments in biological tissues, due to the complex distribution of spectrum types and relaxation times (see Fig. 3), the resulting filtered signals can still contain more signal weighting from certain compartments (intracellular) compared to the others (extracellular, fluid) and thus give some new useful information on the viability of the tissue under study.

Sodium Quantification

Sodium concentration quantification is generally performed by placing phantoms of known sodium concentration and known relaxation times within the field-of-view of the images. It is better to use phantoms with relaxation times that match approximately the relaxation times of the investigated tissue in order to reduce uncertainties in the quantification. A linear regression from the phantom signals, corrected for relaxation, is then applied to produce the tissue sodium concentration (TSC) map. For example, reference phantoms for brain or muscle imaging are composed of 2–3% agar gels with sodium concentrations within the range of TSC usually found in these tissues (10 mM up to 150 mM). For cartilage, 4–6% agar gels can be used, with sodium concentration between 100 to 350 mM.

Limitations and Prospects

Limitations—The low sodium concentration in biological tissues compared to the water concentration, associated with a low NMR sensitivity and very short transverse relaxation times, make the detection of sodium signal quite challenging and result in images with low SNR (around 20–40), low resolution (2–10 mm) and long acquisition times (10–30 min). Moreover, due the low gyromagnetic ratio of the sodium nuclei (26% of proton gyromagnetic ratio), high magnetic field gradients need to be used for acquiring images with higher resolution, which can therefore be limited by the hardware capacities of the clinical scanners (around 40 mT/m in general). This gradient limitation can also impede studies on sodium ions diffusion with MRI due to the very high gradients needed for detecting ion displacements. Other limitations include the need of high static magnetic fields (>3T) for increasing the sodium signal associated with multinuclear capabilities and the availability of single tuned sodium ^{23}Na coils or dual-tuned ^{1}H/^{23}Na RF coils that allow to acquire co-registered proton and sodium images.

Prospects—Sodium MRI acquisitions could profit from new recent multi-channel capabilities developed for rapid proton MRI with parallel data acquisition (array coils) and parallel reconstruction algorithms (62), and also new reconstruction schemes such as compressed sensing (CS), that allow rapid undersampled data acquisitions (63). An optimized combination of parallel-CS-NUFFT reconstruction associated with optimized sequences such as TPI at high field could therefore allow to significantly reduce the acquisition time to a few minutes and still generate images of good resolution (1–2 mm) and reasonable SNR, that would put sodium MRI in the realm of practical clinical imaging techniques. As assessing the intracellular sodium content can give more useful metabolic information on the integrity of cells, techniques that increase the sensitivity of sodium MRI to this specific sodium compartment, such as IR or TQF, still need to be improved in order to increase the SNR, and thus reduce the resolution and acquisition time of the images, as well as reducing their sensitivities to magnetic field and RF inhomogeneities (64). A recent

new method based on optimal control theory (65, 66) could also prove to be useful for this purpose, but it is still under investigation and has not been applied to *in vivo* sodium MRI yet.

BIOMEDICAL APPLICATIONS

In this part we will give an overview of the possible biomedical applications of sodium MRI for assessing diseases and therapies non-invasively and quantitatively *in vivo*. Of course, this list of applications is not exhaustive, but we expect it shows a fair spectrum of the research that has been performed over the last 30 years on this subject.

Brain

Many sodium MRI studies have already been performed on brain to evaluate their possible use for assessing tumors or neurodegenerative diseases (12, 14, 18, 67–71). Examples of SQ and TQF brain sodium images are shown in Fig. 6 A and B.

Stroke—Stroke is the third largest cause of death in the USA and a leading cause of long-term disability and most of the strokes are ischemic (around 87 %). It is very important to intervene as early as possible after symptom onset in order to reperfuse viable tissues and minimize tissue loss for improving recovery. The usual treatment is thrombolysis by intravenous injection of recombinant tissue plasmogen (tPA) within a 3-hour window after onset (72), which induce recanalization of blocked arteries and potentially reperfusion of ischemic tissues. However, there is a risk of hemorrhagic transformation or edema formation due to reperfusion in non-viable tissues which can reverse the expected outcome of thrombolysis. It is therefore very important to assess the viability of tissues and their likelihood to recover before treatment is applied. A combination of proton diffusion weighted imaging (DWI) and perfusion weighted imaging (PWI) (73) has been proposed to help identify patients with more probable improvement in outcome after thrombolysis: ADC maps from DWI can identify regions of cerebral ischemia (water restriction), and PWI can detect regions with perfusion deficits (regions at risk). The mismatch area between a larger abnormal PWI region and a smaller lesion in ADC map is supposed to represent the ischemic penumbra, where the tissue is at risk for infarction but still viable, and therefore could be saved (74–76).

Recent studies in humans (77–80) have shown that an elevation of 50% in TSC above the value in the homologous region in contralateral brain hemisphere was consistent with completed infarction, which corresponds to a value of 70 mM in humans. This value could therefore serve as a threshold for tissue viability. It is also suggested that the different rates of loss of tissue viability are reflected in the different rates of change in TSC values. These studies showed that sodium MRI can be a useful complement to the DWI-PWI mismatch method for managing patients with stroke and that TSC evolution can help guide thrombolysis protocol outside the 3-hour time window. Some examples of sodium images in human stroke are shown in Fig. 6C. In this study, Tsang et al. (81) showed that sodium signal intensity cannot be predicted by PWI and that is was not altered within the PWI-DWI mismatch tissue, indicating preserved viable tissue in this region.

Tumor—Tumor malignancy can be characterized by angiogenesis and cell proliferation. Unregulated cell division, leading to tumor growth, can be initiated by changes in Na^+/H^+ exchange kinetics and therefore changes in the intracellular and extracellular pH (82). This mechanism, associated with altered Na^+/K^+-ATPase activity (83) leads to increased intracellular sodium concentration that can therefore be associated with tumor malignancy (84, 85). Similarly, tumor neovascularization and increase in interstitial space both lead to

increased extracellular volume fraction and are also associated with the potential for tumor proliferation (86). Overall, TSC levels in malignant tumors are likely to be elevated.

The conventional MRI protocol for brain tumor is based on T2 weighted images and T1 weighted images with and without gadolinium enhancement for detecting the location and dimension of the tumor, DWI for detecting the extent of vasogenic edema while excluding cytotoxic edema and PWI for detecting the regions of the tumor with high vascularity, which are consistent with high-grade tumor (87). All these changes are generally late events in tumor onset. Adding sodium MRI to the protocol would therefore provide direct and rapid biochemical information on the tumor metabolism, and also help monitor the effects of cancer therapies over time.

Ouwerkerk et al. (85) combined proton and sodium MRI to measure the TSC in brain and determine how it is altered in malignant tumors. Significant differences in TSC were demonstrated for both tumors and surrounding tissues (+50–60%) versus contralateral brain tissue. However, these measurements cannot define if TSC increases are due to changes in extracellular volume, intracellular sodium content or neovascularization. Nagel et al. (88) recently applied sodium MRI with and without IR to patients with brain tumors of different grades (WHO grades I–IV). Some examples of proton and sodium images are presented in Fig 7 A–F. Their findings were that TSC imaging revealed increased signal intensities in brain tumors and that IR imaging enabled further differentiation of these lesions by suppressing CSF and edema signal. All glioblastomas (grade IV) demonstrated higher IR signal intensities compared to grade I–III tumors. Very recently Fiege et al (89) applied a combination of SQ and TQF sodium imaging to brains with tumors. They detected a decrease of signal in tumor regions on the TQF images compared to normal tissue, probably due to suppression of edema around the tumors. But due to the very low resolution of the images (10 mm isotropic) and low SNR of the TQF images, it is hard to reach any definitive conclusion yet.

Multiple Sclerosis—MS is an inflammatory neurological disease characterized by focal and diffuse inflammation in white matter (WM) and grey matter (GM), by demyelination of the axons, and by neuro-axonal injury and loss (ref). Studies have shown that the accumulation of sodium in axons can promote reverse action of the Na^+/Ca^{2+} exchanger, leading to a metabolic cascade and an overload in intra-axonal calcium, resulting in axon degeneration (90, 91). Inglese et al. (92) recently demonstrated the first application of sodium MRI to MS in patients with advanced relapsing-remitting MS (rrMS). The main results are shown in Fig. 7 G–H. The absolute TSC was measured in lesions and in several areas of proton MRI normal-appearing white and grey matters (NAWM and NAGM) in patients, and corresponding areas in controls. In MS patients, TSC were higher in MS lesions compared to areas of NAWM, and these areas of NAWM were also significantly higher than those in corresponding WM regions in healthy controls. The expanded disability status scale score showed a mild positive association with the mean TSC in chronic lesions, and in regions of NAWM and NAGM. Another recent study by Zaaraoui et al. (93) expanded the method to patients with early and advanced rrMS. It was found that TSC increased inside demyelinated lesions in both groups of patients, and that TSC was increased in NAMW and NAGM of advanced rrMS patients, but not in early rrMS.

Alzheimer's Disease—A first study on the applicability of sodium MRI to Alzheimer's disease (AD) was performed by Mellon et al. (94). The hypothesis is that alterations of the sodium levels in brain due to cell death or loss of viability characteristics of AD could be measured with sodium MRI and give useful complementary information for assessment of early AD. A small increase (7.5%) of the sodium relative signal intensity in the brains of patients with AD was detected compared to controls, but no conclusive explanation on a

physiological basis can be advanced for explaining this increase for the moment, which can be due to many factors such as increase of extracellular volume due to cell death, fluid invasion, intracellular sodium increase or leakage of sodium due to amyloid beta channels in the membrane.

Huntington's Disease—A very recent preliminary study (95) showed that patients with Huntington's disease also present an increased of TSC in the whole brain compared to healthy controls, in structurally affected regions of the brain, but also in some non-affected regions.

Breast

Treatments for breast cancer such as prophylactic mastectomy or chemoprevention are more effective when the disease is detected at an early stage. X-ray mammography has a high sensitivity but can lead to many false positives (30%) (96), and very often cannot distinguish benign from malignant tumors. Moreover, many tumors cannot not detected by mammography due to the presence of dense fibroglandular tissue. Proton MRI is promising technique for detecting and characterizing tumors not visible in mammograms (97), mainly in dense tissues, and its specificity could be improved by adding more information about the metabolism of suspicious lesions. To test this hypothesis, Ouwerkerk et al (98) applied sodium MRI to patients with benign and malignant breast tumors before biopsy. The measured TSC were higher by an average of 60% in histologically proven malignant lesions compared to glandular tissue. TSC in benign tumors was significantly higher than adipose tissue but on the same level as the glandular tissue. An example of these results is shown in Fig. 8. It is impossible from this data to reach any conclusion about the origins of the measured elevated TSC, but more studies with a combination of sodium sequences allowing to increase the weight of intracellular sodium on the images (such as TQF or IR), combined with proton DWI or contrast enhanced MRI, may allow to increase the sensitivity and specificity of breast cancer MRI. It was even shown recently by Jacobs et al. (99) that a multimodal combination of ^{1}H+^{23}Na MRI with computed tomography (CT) and proton emission tomography (PET) was feasible and may help to evaluate the complex tumor micro-environment by examining changes in morphology, sodium concentrations and glucose metabolism in response therapy.

Heart

Acute myocardial infarction (MI) can lead to an increase in the intracellular sodium concentration due to loss of ionic homeostasis, and to enlarged extracellular volume due to myocardial edema formation or scar formation (100, 101). Some preliminary studies were performed over the years to test the feasibility of cardiac sodium MRI and to try to assess infarction (102–106). Ouwerkerk et al. (104) measured the myocardial TSC of healthy volunteers and in patients with nonacute MI. Mean TSC for MI was measured as 30% higher than non-infarcted tissues. The mean TSC in regions adjacent to MI regions was intermediate between MI and normal tissue. These measured sodium intensity changes may be attributable to loss of cellular integrity and also possibly changes in the sodium ion molecular environment.

Muscle

In muscle tissues, the electrochemical gradient across the cell membrane is maintained by the Na^+/K^+/ATPase, but when an action potential leading to muscle contraction is generated, there is a rapid influx of sodium ions and efflux of potassium ions via the sodium and potassium channels. During intense contractile activity, the persistent influx and efflux of ions can lead to a loss of membrane excitability and muscle contractility (107), which is

believed to represent one of the main mechanisms of muscle fatigue (108). Many disease states, such as diabetes, starvation and hypothyroidism, can be linked to a decrease in Na^+/K^+-ATPase activity in skeletal muscle (107). Bansal et al. (109) studied the change of sodium concentration and relaxation in muscle after voluntary muscle contractions. They detected an increase of the sodium intensity in the images by around 34% in the exercised muscle and then a decrease with a half-time of 30 min, but could not confirm a change in TSC due to changes in the T2 of the slow relaxing component and the long TE of the imaging method (5 ms). These changes in T2 are likely caused by vascular and osmotic changes that alter the microenvironment of the observed sodium ions.

Diabetes—Some results from the study by Chang et al. (110) are presented in Fig. 9. Pre- and post-exercise sodium intensity (SI) was measured in healthy volunteers and patients with diabetes, in the tibialis anterior (TA) as control muscle, in soleus (S) and in gastrocnemius (G) muscles. It was found that the SI in S and G increased significantly immediately after exercise and that afterwards this SI recovered down to baseline more slowly in diabetics than in healthy subjects. Possible explanations might be the altered tissue microvasculature in diabetics, as well as a decreased Na^+/K^+/ATPase activity and decreased numbers of Na^+ and K^+ pumps on the muscle cell membrane, which has been attributed to insulin resistance (111). This latter mechanism would result in a decreased ability to extrude intracellular sodium ions into the extracellular space and result in persistently elevated muscle sodium intracellular content with a slower recovery to baseline.

Muscular Channelopathy—Patients with hypokalemic periodic paralysis (hypoPP) or paramyotonia congenita (PC), two different kinds of muscular channelopathies, were scanned with sodium MRI in a study by Nagel et al. (112). These rare diseases are considered to be caused by genetic mutations of the voltage-gated sodium channels in muscular cells, and can be characterized by elevated myoplasmic sodium at rest and after cooling (for provoking PC pathology effects). Three sodium techniques were used: total tissue sodium concentration (23Na-TSC), T1 weighted sodium imaging (23Na-T1) and inversion recovery (23Na-IR) for suppressing most of the extracellular and vascular sodium and vasogenic edema. All sequences showed significantly higher signal intensities in hypoPP compared with PC patients and healthy subjects. Provocation in PC induced a significant increase in the 23Na-IR signal and a corresponding decrease of muscle strength. This study indicates that 23Na-IR could provide a stronger weighting toward intracellular sodium than 23Na-T1 or 23Na-TSC. The same kind of study was performed on patient with hyperkalemic periodic paralysis (hyperPP) by Armateifo et al. (113). It was shown that sodium MRI can detect increased myoplasmic sodium content in HyperPP patients with permanent weakness, as they are affected by an incomplete inactivation of muscular sodium channels (114).

Myotonic Dystrophy—Myotonic dystrophy has been linked to alterations in sodium channel conductance regulation, which can cause elevated muscle fiber concentrations that correlate with disease severity (115). For example, Constantinides et al. (116) found that the mean TSC measured with sodium MRI after exercise were elevated by around 20% in two healthy volunteers, and 47% and 70% in two dystrophic muscles compared with those at normal resting levels, which is consistent with the known imbalance in sodium homeostasis in dystrophic muscle fibers (117).

Hypertension—Another interesting possible application of quantitative sodium MRI in muscle is to measure the increase of body sodium content due to hypertension, which is linked to a disturbed total body sodium regulation. Kopp et al. (118) measured sodium content in triceps surae of healthy volunteers and of patients with primary aldosteronism, a

cause of hypertension, before and after treatment. They found a 29% increase in muscle Na^+ content in patients with aldosteronism compared to normal volunteers. This tissue Na^+ content was then reduced to normal levels (20–25 mM) after treatment. They suggest that sites such as muscle (and also skin) could serve to store Na^+ non-osmotically by binding of the Na^+ ion to proteoglycans within the extracellular compartment without apparent accompanying fluid retention or changes in serum Na^+ concentration in patients with primary aldosteronism.

Cartilage

Cartilage is a dense connective tissue that can be found in articular joints between bones, in the ear and nose or in intervertebral disk. Articular hyaline cartilage consists of a small population of chondrocytes (5% of volume) within a large extracellular matrix (ECM) made of collagen fibers (15–20% of the volume), proteoglycans (PG; 3–10%) and water (65–80%) and does not contain blood vessels. PGs further contain negatively charged glycosaminoglycan (GAG) chains, which endow the cartilage with a negative fixed charge density (FCD). This FCD attracts free-floating $^{23}Na^+$ ions, which in turn attract water molecules within the cartilage through osmotic pressure. Therefore, unlike most of biological tissues, sodium ions in cartilage are mostly present in the extracellular volume. The negative charge from the GAG chains also provides a strong electrostatic repulsive force between the PG molecules and is responsible for the compressive stiffness of cartilage (24).

Osteoarthritis—Osteoarthritis (OA) is the most common form of arthritis in synovial joints and a leading cause of chronic disability in the elderly population. OA is a degenerative disease of the articular cartilage mainly characterized by a reduction of FCD (or GAG) concentration, possible changes of size and organization of the collagen fibers, aggregation of the PG and increased water content. These changes lead to an alteration of the mechanical properties of the cartilage, which can therefore lose its load- and shear-bearing functions. Radiography is the standard method used to detect gross loss of cartilage by measuring narrowing of the distance between the two adjacent bones of a joint, but does not image cartilage directly. T1-weighted, T2-weighted and proton density MRI can provide morphological information on damage of cartilage, but do not give any information on the GAG content or on the ECM structure. New methods for functional proton MRI of the cartilage are under now development, such as T1ρ mapping (119), T2 mapping (120), GAG chemical exchange saturation transfer (gagCEST) (121), delayed gadolinium enhanced MRI of cartilage (dGEMRIC) (122) and diffusion weighted imaging (DWI) (123). It has also been shown that sodium concentration has a strong correlation with FCD and GAG content in cartilage (124), so quantitative sodium MRI could also be useful for detecting directly loss of GAG in early OA (125–127). Several studies have already been performed on healthy and OA cartilage, and show that in general TSC in healthy cartilage is in the range 250–350 mM, while it is <250 mM in OA cartilage (127). Because of the low resolution of the sodium images (>3 mm), due to the presence of synovial fluid or joint effusion and also cartilage thickening, the sensitivity of the method to measure small changes of TSC within the cartilage should include fluid suppression by either TQF (17, 128) or IR (129). An example of sodium MRI of cartilage in presented in Fig. 10, where fluid suppression was obtained by adiabatic IR (54).

Cartilage Repair—Trattnig et al. (130) showed the feasibility of dGEMRIC and sodium MRI for differentiating repaired tissue after matrix-associated autologous chondrocyte transplantation (MACT) from native cartilage. A strong correlation was found between sodium imaging and dGEMRIC in patients after MACT. Another recent study by Chang et

al. (131) showed that the method for assessing sodium concentration in cartilage repair can be improved by fluid suppression by IR.

Intervertebral Disc—Insko et al. (132) demonstrated the feasibility of sodium MRI of the intervertebral disk (IVD) *in vivo.* This technique could be used to measure the proteoglycan content in the fibrocartilage and help detect early degenerative changes in IVD.

Abdomen

Quantitative sodium MRI could also be useful for assessing cell viability in abdominal organs and diagnosing diseases in liver, gallbladder, pancreas, kidney, spleen, prostate, uterus or other organs but very few studies have been performed for the moment on the abdomen, mainly due to the lack of availability of body sodium coils.

Kidney—The kidney is essential in regulating homeostatic functions in the body such as extracellular fluid volume, pH balance, electrolyte concentrations, and blood pressure. This role depends on the regulation of extracellular sodium in the kidney, which builds up a concentration gradient from the cortex to the medulla. A first study in human by Maril et al. (133) present sodium MRI of kidneys before after water deprivation, as shown in Fig. 11. The results show that the sodium signal intensity increased linearly from the cortex to each of the medullae and then decreased toward the renal pelvis. After 12 hour water deprivation, this gradient increased significantly by 25%. The sodium gradient change in the kidney may reflect changes in the concentration in each kidney compartment (cortex, medulla), but also micro-compartments within these compartments (intracellular, extracellular, vascular). A following study by Rosen et al. (134) performed sodium MRI on a patient with a transplanted kidney, who was previously diagnosed with end-stage hypertensive nephropathy. The gradient slope was lower than the gradient slope observed in healthy kidney in the previous study. A interpretation cannot be made at this stage as the kidney was recently transplanted, resolution and SNR were low and the physiology/biochemistry involved are not fully known. More studies need to be done of course, but these findings are encouraging for a possible application of quantitative sodium MRI for assessing renal functions in different diseases such as nephropathy, renal failure and kidney transplantation.

Prostate—Sodium MRI of the human prostate was recently tested *in vivo* (135). The prostate and its different departments were identifiable, with measured TSC of around 60 mM in the central zone and 70 mM in the peripheral zone. This method could be a potential radiological biomarker of prostate cancer.

Uterus—Uterine leiomyomata (fibroids) were investigated by DWI and sodium MRI by Jacobs et al. (136). Uterine leiomyomata are solid masses arising from the muscle of the uterus (myometrium) and can be associated with menstrual pain and loss of reproductive function. Regions where the tissue was treated with high-intensity focused ultrasound surgery were clearly identified on both DWI and sodium images. TSC decreased in untreated fibroids and increased in treated fibroids compared to normal tissue, while ADC decreased in untreated fibroids, and continued to decrease even more in treated fibroids, compared to normal tissue. Thermal ablation disrupts the cell membrane and alters perfusion of the tissue. The ADC and sodium changes within the diseased uterine tissue before and after treatment may therefore reflect a combination of complex changes in tissues such as modification of the water environment, disruption of Na^+/K^+-ATPase function, decreased vascularization or cytotoxic edema.

Whole Body

Most of human parts have been scanned with sodium MRI separately, but a recent study by Wetterling et al. (137) showed a whole body sodium MRI. The resulting composite image of 5 acquisitions of 10 min each is shown in Fig. 12. A possible application of whole body sodium imaging would be for example the detection and malignancy assessment of cancer with metastases.

Cancer and Chemotherapeutic Response

Although the following studies were not performed on humans but on rats or mice *in vivo*, it is useful to mention them as they represent an important preliminary work previous to potential human applications on cancer and chemotherapeutic response assessment (55, 138, 139). The goal of cancer therapy is to eliminate neoplastic cells, but assessment of the therapeutic efficiency *in vivo* may be difficult.

Chemotherapy Assessment—DWI can be useful for quantitative assessment of tumor response to therapeutic insult by observing the changes in water diffusion due to cellular destruction and it is highly sensitive to microscopic changes in cellular structure (140). These microscopic changes generally precede macroscopic changes in tumor volume, which occur at much later stages after therapeutic insult. On the other hand, quantitative sodium MRI can give direct information on the integrity of the cell membrane and cellular energy consumption. Schepkin et al. (141) studied the possibility of using DWI and sodium MRI for assessing the effect of chemotherapeutic treatment of tumors *in vivo*. The study was performed on 9L gliosarcomas implanted in rats and then treated with varying doses of BCNU. Main results are shown in Fig. 13 A–B. This study demonstrate that there is a good correlation between DWI and sodium MRI in their ability to reveal the efficacy of tumor therapy in a few days following treatment in a dose dependent manner.

Babsky et al. (142) implanted fibrosarcoma tumors in mice and monitored the effects of 5-fluorouracil (5FU) treatment with proton DWI, SQ and TQF sodium MRI, and positron emission tomography (PET) for measuring Fluorodeoxyglucose (FDG) uptake in the tumor. They found that the correlated increases in SQ sodium intensity and water ADC following chemotherapy in tumors might reflect an increase in extracellular space, while the lower TQF sodium signal and FDG uptake in treated tumors compared with control tumors suggest a shift in tumor metabolism from glycolysis to oxidation and/or a decrease in cell density.

Kline et al. (55) used sodium MRI with IR to monitor the response to chemotherapy of mouse xenograft tumors propagated from human prostate cancer cell lines. A 37% increase in sodium signal intensity in tumors was observed after administration of antineoplastics, which can be matched with the results of experiments with these same drugs and cells treated in culture, where a significant intracellular sodium elevation was detected using a fluorescent dye. Sodium MRI with IR seems to increase the weight of the images to intracellular sodium and could therefore help monitoring non-invasively apoptosis of tumors cells induced by chemotherapy.

Tumor Resistance to Therapy—Schepkin et al. (143) also studied the capability of sodium MRI and DWI for monitoring the tumor resistance to chemotherapy in intracranial rat 9L gliomas. It was measured that implanted resistant 9L cells created tumors with significantly reduced TSC than nonresistant (naive) 9L cells and that corresponding differences in ADC were less pronounced but still significant. The main results are presented in Fig. 13 C–D. Both sodium content and ADC can differentiate resistant from naive tumors, but they vary at very different rates in the two kinds of tumors after treatment, and thus must depends on different mechanisms. This study shows that TSC could give

important information about the level of drug resistance before chemotherapy and that it is more sensitive than DWI for detecting small changes in tumor resistance.

CONCLUSION

We have shown that sodium MRI can help assess directly, in a non-invasive and quantitative manner, some important new metabolic information such as tissue viability, through cell integrity and energy status, and that this information cannot be determined by standard anatomical or functional proton MRI or other non-invasive imaging modality.

From the research point of view, there is an increasing interest in this technique, as more and more tissues and diseases are investigated, from brain tumors and strokes to osteoarthritis in articular cartilage, passing through kidney impairments and diabetes in muscles. However, more research still needs to be on both software and hardware for improving the data acquisitions and reconstructions, and increasing the sensitivity of the technique to specific sodium parameters (e.g. intracellular sodium or relaxation times).

From the medical point of view, more research still has to be performed *in vivo*, on more patients with diseases (longitudinal studies) or healthy subjects (optimization of data acquisitions and reconstruction, combined single and multiple quantum sodium imaging) in order to convince radiologist/physicians that sodium MRI could add some crucial information for the diagnosis but also prognosis of diseases, as a complement to more developed techniques such as DTI or PWI, for the management of patients (e.g. with stroke) or about the possible outcomes of treatments (chemotherapy resistance).

And last but not least, from the commercial point of view, sodium MRI cannot become a clinical tool without the help of the major scanner vendors which should help develop multichannel-multinuclear hardware, new multi-tuned RF coils and new UTE sequences and reconstruction algorithms along with the availability of high magnetic fields (>3T).

Acknowledgments

Grant Support

This work was partly supported by research grants (RO1 AR053133, RO1 AR056260, and RO1 AR060238), from the National Institute of Arthritis and Musculoskeletal and Skin Diseases (NIAMS), National Institutes of Health (NIH).

References

1. Sodium in health and disease. New York: Informa Healthcare USA, Inc;
2. Murphy E, Eisner DA. Regulation of intracellular and mitochondrial sodium in health and disease. Circulation Research. 2009; 104(3):292–303. [PubMed: 19213964]
3. Rose AM, Valdes R. Understanding the Sodium-Pump and Its Relevance to Disease. Clinical Chemistry. 1994; 40(9):1674–85. [PubMed: 8070076]
4. Skou JC, Esmann M. The Na, K-Atpase. J Bioenerg Biomembr. 1992; 24(3):249–61. [PubMed: 1328174]
5. Bloch F, Hansen WW, Packard M. Nuclear Induction. Phys Rev. 1946; 69(3–4):127.
6. Purcell EM, Torrey HC, Pound RV. Resonance Absorption by Nuclear Magnetic Moments in a Solid. Phys Rev. 1946; 69(1–2):37–8.
7. Berendsen HJ, Edzes HT. The observation and general interpretation of sodium magnetic resonance in biological material. Annals of the NewYork Academy of Sciences. 1973; 204:459–85.
8. Magnuson JA, Magnuson NS. NMR studies of sodium and potassium in various biological tissues. Annals of the New York Academy of Sciences. 1973; 204:297–309. [PubMed: 4513156]

9. Feinberg DA, Crooks LA, Kaufman L, et al. Magnetic resonance imaging performance: a comparison of sodium and hydrogen. Radiology. 1985; 156(1):133–8. [PubMed: 4001399]
10. Maudsley AA, Hilal SK. Biological Aspects of Na-23 Imaging. Brit Med Bull. 1984; 40(2):165. [PubMed: 6744003]
11. Moseley ME, Chew WM, Nishimura MC, et al. In vivo sodium-23 magnetic resonance surface coil imaging: observing experimental cerebral ischemia in the rat. Magnetic Resonance Imaging. 1985; 3(4):383–7. [PubMed: 4088012]
12. Hilal SK, Maudsley AA, Ra JB, et al. In vivo NMR imaging of sodium-23 in the human head. Journal of computer assisted tomography. 1985; 9(1):1–7. [PubMed: 3968256]
13. Ra JB, Hilal SK, Oh CH, Mun IK. In vivo magnetic resonance imaging of sodium in the human body. Magn Reson Med. 1988; 7(1):11–22. [PubMed: 3386516]
14. Grodd W, Klose U. Sodium-MR-imaging of the brain: initial clinical results. Neuroradiology. 1988; 30(5):399–407. [PubMed: 2850509]
15. Boada FE, Gillen JS, Shen GX, Chang SY, Thulborn KR. Fast three dimensional sodium imaging. Magn Reson Med. 1997; 37(5):706–15. [PubMed: 9126944]
16. Wimperis S, Wood B. Triple-Quantum Sodium Imaging. J Magn Reson. 1991; 95(2):428–36.
17. Borthakur A, Hancu I, Boada FE, Shen GX, Shapiro EM, Reddy R. In vivo triple quantum filtered twisted projection sodium MRI of human articular cartilage. J Magn Reson. 1999; 141(2):286–90. [PubMed: 10579951]
18. Hancu I, Boada FE, Shen GX. Three-dimensional triple-quantum-filtered(23)Na imaging of in vivo human brain. Magn Reson Med. 1999; 42(6):1146–54. [PubMed: 10571937]
19. Jaccard G, Wimperis S, Bodenhausen G. Multiple-Quantum Nmr-Spectroscopy of S=3/2 Spins in Isotropic-Phase -a New Probe for Multiexponential Relaxation. JChemPhys. 1986; 85(11):6282–93.
20. Van der Maarel JRC. Thermal relaxation and coherence dynamics of spin 3/2. I. Static and fluctuating quadrupolar interactions in the multipole basis. Concept Magn Reson A. 2003; 19A(2): 97–116.
21. Bowden GJ, Hutchison WD, Khachan J. Tensor Operator-Formalism for Multiple-Quantum NMR. 2. Spins-3/2, Spin-2, and Spin-5/2 and General-I. J MagnReson. 1986; 67(3):415–37.
22. Bowden GJ, Hutchison WD. Tensor Operator-Formalism for Multiple-Quantum NMR. 1. Spin-1 Nuclei. J Magn Reson. 1986; 67(3):403–14.
23. Rooney WD, Springer CS. A Comprehensive Approach to the Analysis and Interpretation of the Resonances of Spins 3/2 from Living Systems. NMR Biomed. 1991; 4(5):209–26. [PubMed: 1751345]
24. Borthakur A, Mellon E, Niyogi S, Witschey W, Kneeland JB, Reddy R. Sodium and T1rho MRI for molecular and diagnostic imaging of articular cartilage. NMR Biomed. 2006; 19(7):781–821. [PubMed: 17075961]
25. Rooney WD, Springer CS Jr. The molecular environment of intracellular sodium: 23Na NMR relaxation. NMR Biomed. 1991; 4(5):227–45. [PubMed: 1751346]
26. Kemp-Harper R, Brown SP, Hughes CE, Styles P, Wimperis S. Na-23 NMR methods for selective observation of sodium ions in ordered environments (vol 30, pg 157, 1997). Prog Nucl Mag Res Spec. 1997; 31:287.
27. Parrish TB, Fieno DS, Fitzgerald SW, Judd RM. Theoretical basis forsodium and potassium MRI of the human heart at 1.5 T. Magn Reson Med. 1997; 38(4):653–61. [PubMed: 9324333]
28. Nielles-Vallespin S, Weber MA, Bock M, et al. 3D radial projection technique with ultrashort echo times for sodium MRI: clinical applications in human brain and skeletal muscle. Magn Reson Med. 2007; 57(1):74–81. [PubMed: 17191248]
29. Nagel AM, Laun FB, Weber MA, Matthies C, Semmler W, Schad LR. Sodium MRI using a density-adapted 3D radial acquisition technique. Magn Reson Med. 2009; 62(6):1565–73. [PubMed: 19859915]
30. Boada FE, Shen GX, Chang SY, Thulborn KR. Spectrally weighted twisted projection imaging: reducing T2 signal attenuation effects in fast three-dimensional sodium imaging. Magn Reson Med. 1997; 38(6):1022–8. [PubMed: 9402205]

31. Lu AM, Atkinson IC, Claiborne TC, Damen FC, Thulborn KR. Quantitative Sodium Imaging With a Flexible Twisted Projection Pulse Sequence. Magnet Reson Med. 2010; 63(6):1583–93.
32. Gurney PT, Hargreaves BA, Nishimura DG. Design and analysis of a practical 3D cones trajectory. Magn Reson Med. 2006; 55(3):575–82. [PubMed: 16450366]
33. Pipe JG, Zwart NR, Aboussouan EA, Robison RK, Devaraj A, Johnson KO. A new design and rationale for 3D orthogonally oversampled k-space trajectories. Magn Reson Med. 2011; 66(5): 1303–11. [PubMed: 21469190]
34. Romanzetti S, Halse M, Kaffanke J, Zilles K, Balcom BJ, Shah NJ. A comparison of three SPRITE techniques for the quantitative 3D imaging of the Na-23 spin density on a 4T whole-body machine. J Magn Reson. 2006; 179(1):64–72. [PubMed: 16325438]
35. Balcom BJ, MacGregor RP, Beyea SD, Green DP, Armstrong RL, Bremner TW. Single-point ramped imaging with T-1 enhancement (SPRITE). J Magn Reson Ser A. 1996; 123(1):131–4. [PubMed: 8980075]
36. Idiyatullin D, Corum C, Park JY, Garwood M. Fast and quiet MRI using a swept radiofrequency. J Magn Reson. 2006; 181(2):342–9. [PubMed: 16782371]
37. Weiger M, Pruessmann KP, Hennel F. MRI with Zero Echo Time: Hard versus Sweep Pulse Excitation. Magnet Reson Med. 2011; 66(2):379–89.
38. Grodzki DM, Jakob PM, Heismann B. Ultrashort echo time imaging using pointwise encoding time reduction with radial acquisition (PETRA). Magnet Reson Med. 2012; 67(2):510–8.
39. Osullivan JD. A Fast Sinc Function Gridding Algorithm for Fourier Inversion in Computer-Tomography. IEEE Trans Med Imag. 1985; 4(4):200–7.
40. Sedarat H, Nishimura DG. On the optimality of the gridding reconstruction algorithm. IEEE Trans Med Imag. 2000; 19(4):306–17.
41. Schomberg H, Timmer J. The gridding method for image reconstruction by Fourier transformation. IEEE Trans Med Imag. 1995; 14(3):596–607.
42. Fessler JA. On NUFFT-based gridding for non-Cartesian MRI. J Magn Reson. 2007; 188(2):191–5. [PubMed: 17689121]
43. Greengard L, Lee JY. Accelerating the nonuniform fast Fourier transform. Siam Rev. 2004; 46(3): 443–54.
44. Navon G, Shinar H, Eliav U, Seo Y. Multiquantum filters and order in tissues. NMR Biomed. 2001; 14(2):112–32. [PubMed: 11320537]
45. Chung CW, Wimperis S. Optimum Detection of Spin-3/2 Biexponential Relaxation Using Multiple-Quantum Filtration Techniques. J Magn Reson. 1990; 88(2):440–7.
46. Bodenhausen G. Multiple-Quantum Nmr. Prog Nucl Mag Res Spec. 1980; 14:137–73.
47. Reddy R, Shinnar M, Wang Z, Leigh JS. Multiple-Quantum Filters of Spin-3/2 with Pulses of Arbitrary Flip Angle. J Magn Reson Ser B. 1994; 104(2):148–52. [PubMed: 8049867]
48. Hutchison RB, Shapiro JI. Measurement of intracellular sodium with NMR methods. Concepts Magn Reson. 1991; 3:215–63.
49. Gupta RK, Gupta P, Moore RD. NMR-Studies of Intracellular Metal-Ions in Intact-Cells and Tissues. Annu Rev Biophys Bio. 1984; 13:221–46.
50. Naritomi H, Kanashiro M, Sasaki M, Kuribayashi Y, Sawada T. Invivo Measurements of Intracellular and Extracellular Na+ and Water in the Brain and Muscle by Nuclear-Magnetic-Resonance Spectroscopy with Shift-Reagent. Biophys J. 1987; 52(4):611–6. [PubMed: 3676441]
51. Winter PM, Bansal N. TmDOTP5- as a Na-23 shift reagent for the subcutaneously implanted 9L gliosarcoma in rats. Magnet Reson Med. 2001; 45(3):436–42.
52. van der Veen JW, van Gelderen P, Creyghton JH, Bovee WM. Diffusion in red blood cell suspensions: separation of the intracellular and extracellular NMR sodium signal. Magn Reson Med. 1993; 29(4):571–4. [PubMed: 8464377]
53. Stobbe R, Beaulieu C. In vivo sodium magnetic resonance imaging of the human brain using soft inversion recovery fluid attenuation. Magn Reson Med. 2005; 54(5):1305–10. [PubMed: 16217782]
54. Madelin G, Lee JS, Inati S, Jerschow A, Regatte RR. Sodium inversion recovery MRI of the knee joint in vivo at 7T. J Magn Reson. 2010; 207(1):42–52. [PubMed: 20813569]

55. Kline RP, Wu EX, Petrylak DP, et al. Rapid in vivo monitoring of chemotherapeutic response using weighted sodium magnetic resonance imaging. Clinic Cancer Res. 2000; 6(6):2146–56.
56. Navon G. Complete Elimination of the Extracellular Na-23 Nmr Signal in Triple Quantum Filtered Spectra of Rat Hearts in the Presence of Shift-Reagents. Magnet Reson Med. 1993; 30(4):503–6.
57. Eliav U, Shinar H, Navon G. The Formation of a 2nd-Rank Tensor in Na-23 Double-Quantum-Filtered Nmr as an Indicator for Order in a Biological Tissue. J Magn Reson. 1992; 98(1):223–9.
58. Pekar J, Leigh JS. Detection of Biexponential Relaxation in Na-23 Facilitated by Double-Quantum Filtering. J Magn Reson. 1986; 69(3):582–4.
59. Pekar J, Renshaw PF, Leigh JS. Selective Detection of Intracellular Sodium by Coherence-Transfer Nmr. J Magn Reson. 1987; 72(1):159–61.
60. Jelicks LA, Gupta RK. On the Extracellular Contribution to Multiple Quantum Filtered Na-23 Nmr of Perfused Rat-Heart. Magnet Reson Med. 1993; 29(1):130–3.
61. Jelicks LA, Gupta RK. Double-Quantum Nmr of Sodium-Ions in Cells and Tissues - Paramagnetic Quenching of Extracellular Coherence. J Magn Reson. 1989; 81(3):586–92.
62. Ying L, Liang ZP. Parallel MRI Using Phased Array Coils. Ieee Signal Proc Mag. 2010; 27(4):90–8.
63. Lustig M, Donoho D, Pauly JM. Sparse MRI: The application of compressed sensing for rapid MR imaging. Magnet Reson Med. 2007; 58(6):1182–95.
64. Fleysher L, Oesingmann N, Inglese M. B(0) inhomogeneity-insensitive triple-quantum-filtered sodium imaging using a 12-step phase-cycling scheme. NMR Biomed. 2010; 23(10):1191–8. [PubMed: 20677213]
65. Lee JS, Regatte RR, Jerschow A. Optimal control NMR differentiation between fast and slow sodium. Chem Phys Lett. 2010; 494(4–6):331–6.
66. Lee JS, Regatte RR, Jerschow A. Optimal excitation of Na-23 nuclear spins in the presence of residual quadrupolar coupling and quadrupolar relaxation. J Chem Phys. 2009; 131(17)
67. Boada FE, LaVerde G, Jungreis C, Nemoto E, Tanase C, Hancu I. Loss of cell ion homeostasis and cell viability in the brain: what sodium MRI can tell us. Current Topics in Developmental Biology. 2005; 70:77–101. [PubMed: 16338338]
68. Ouwerkerk R. Sodium MRI. Methods Mol Biol. 2011; 711:175–201. [PubMed: 21279602]
69. Hashimoto T, Ikehira H, Fukuda H, et al. In vivo sodium-23 MRI in brain tumors: evaluation of preliminary clinical experience. Am JPhysiol Imag. 1991; 6(2):74–80.
70. Winkler SS. Sodium-23 magnetic resonance brain imaging. Neuroradiology. 1990; 32(5):416–20. [PubMed: 2259436]
71. Tsang A, Stobbe RW, Beaulieu C. Triple-quantum-filtered sodium imaging of the human brain at 4.7 T. Magn Reson Med. 2012; 67(6):1633–43. [PubMed: 21956282]
72. Tissue plasminogen activator for acute ischemic stroke. The National Institute of Neurological Disorders and Stroke rt-PA Stroke Study Group. New EnglandJMed. 1995; 333(24):1581–7.
73. Luypaert R, Boujraf S, Sourbron S, Osteaux M. Diffusion and perfusion MRI: basic physics. European JRadiol. 2001; 38(1):19–27. [PubMed: 11287161]
74. Schlaug G, Benfield A, Baird AE, et al. The ischemic penumbra: operationally defined by diffusion and perfusion MRI. Neurology. 1999; 53(7):1528–37. [PubMed: 10534263]
75. Neumann-Haefelin T, Wittsack HJ, Wenserski F, et al. Diffusion- and perfusion-weighted MRI. The DWI/PWI mismatch region in acute stroke. Stroke. 1999; 30(8):1591–7. [PubMed: 10436106]
76. Ueda T, Yuh WT, Taoka T. Clinical application of perfusion and diffusion MR imaging in acute ischemic stroke. J Magn ResonImaging. 1999; 10(3):305–9.
77. Boada FE, Qian YX, Nemoto E, et al. Sodium MRI and the Assessment of Irreversible Tissue Damage During Hyper-Acute Stroke. Transl Stroke Res. 2012; 3(2):236–45.
78. Hussain MS, Stobbe RW, Bhagat YA, et al. Sodium imaging intensity increases with time after human ischemic stroke. Annals Neurol. 2009; 66(1):55–62.
79. Thulborn KR, Gindin TS, Davis D, Erb P. Comprehensive MR imaging protocol for stroke management: Tissue sodium concentration as a measure of tissue viability in nonhuman primate studies and in clinical studies. Radiology. 1999; 213(1):156–66. [PubMed: 10540656]

80. Thulborn KR, Davis D, Snyder J, Yonas H, Kassam A. Sodium MR imaging of acute and subacute stroke for assessment of tissue viability. Neuroimag Clin N Am. 2005; 15(3):639.
81. Tsang A, Stobbe RW, Asdaghi N, et al. Relationship between sodium intensity and perfusion deficits in acute ischemic stroke. J Magn ResonImaging. 2011; 33(1):41–7.
82. Rotin D, Steelenorwood D, Grinstein S, Tannock I. Requirement of the Na+/H+ Exchanger for Tumor-Growth. Cancer Res. 1989; 49(1):205–11. [PubMed: 2535690]
83. Spector M, O'Neal S, Racker E. Phosphorylation of the beta subunit of Na+K+-ATPase in Ehrlich ascites tumor by a membrane-bound protein kinase. JBiolChem. 1980; 255(18):8370–3.
84. Cameron IL, Smith NKR, Pool TB, Sparks RL. Intracellular Concentration of Sodium and Other Elements as Related to Mitogenesis and Oncogenesis Invivo. Cancer Research. 1980; 40(5):1493–500. [PubMed: 7370987]
85. Ouwerkerk R, Bleich KB, Gillen JS, Pomper MG, Bottomley PA. Tissue sodium concentration in human brain tumors as measured with Na-23 MR imaging. Radiology. 2003; 227(2):529–37. [PubMed: 12663825]
86. Weidner N. Tumor angiogenesis: review of current applications in tumor prognostication. Seminars in Diagnostic Pathology. 1993; 10(4):302–13. [PubMed: 7511250]
87. Thulborn KR, Lu AM, Atkinson IC, Damen F, Villano JL. Quantitative Sodium MR Imaging and Sodium Bioscales for the Management of Brain Tumors. Neuroimag Clin N Am. 2009; 19(4):615.
88. Nagel AM, Bock M, Hartmann C, et al. The potential of relaxation-weighted sodium magnetic resonance imaging as demonstrated on brain tumors. Invest Radiol. 2011; 46(9):539–47. [PubMed: 21577129]
89. Fiege DP, Romanzetti S, Mirkes CC, Brenner D, Shah NJ. Simultaneous single-quantum and triple-quantum-filtered MRI of 23Na (SISTINA). Magn ResonMed. 2012
90. Waxman SG. Mechanisms of Disease: sodium channels and neuroprotection in multiple sclerosis - current status. Nat Clin Pract Neuro. 2008; 4(3):159–69.
91. Waxman SG, Craner MJ, Black JA. Na+ channel expression along axons in multiple sclerosis and its models. Trends Pharmacol Sci. 2004; 25(11):584–91. [PubMed: 15491781]
92. Inglese M, Madelin G, Oesingmann N, Babb JS, Wu W, Stoekel B, Herbert J, Johnson G. Brain tissue sodium concentration in multiple sclerosis: a sodium iamging study at 3 Tesla. Brain. 2010; 133(3):847–57. [PubMed: 20110245]
93. Zaaraoui W, Konstandin S, Audoin B, et al. Distribution of Brain Sodium Accumulation Correlates with Disability in Multiple Sclerosis: A Cross-sectional 23Na MR Imaging Study. Radiology. 2012; 264(3):859–67. [PubMed: 22807483]
94. Mellon EA, Pilkinton DT, Clark CM, et al. Sodium MR imaging detection of mild Alzheimer disease: preliminary study. Am J Neuroradiol. 2009; 30(5):978–84. [PubMed: 19213826]
95. Reetz K, Romanzetti S, Dogan I, et al. Increased brain tissue sodium concentration in Huntington's Disease -A sodium imaging study at 4T. Neuroimage. 2012; 63(1):517–24. [PubMed: 22796981]
96. Gotzsche PC, Nielsen M. Screening for breast cancer with mammography. Cochrane Db Syst Rev. 2009; (4)
97. Warner E, Messersmith H, Causer P, Eisen A, Shumak R, Plewes D. Systematic review: Using magnetic resonance imaging to screen women at high risk for breast cancer. Ann Intern Med. 2008; 148(9):671–9. [PubMed: 18458280]
98. Ouwerkerk R, Jacobs MA, Macura KJ, et al. Elevated tissue sodium concentration in malignant breast lesions detected with non-invasive Na-23 MRI. Breast Cancer Research and Treatment. 2007; 106(2):151–60. [PubMed: 17260093]
99. Jacobs MA, Ouwerkerk R, Wolff AC, et al. Monitoring of neoadjuvant chemotherapy using multiparametric, (2)(3)Na sodium MR, and multimodality (PET/CT/MRI) imaging in locally advanced breast cancer. Breast Cancer Research and Treatment. 2011; 128(1):119–26. [PubMed: 21455671]
100. Jansen MA, Nederhoff MGJ, Van Echteld CJA. Intracellular sodium magnetic resonance imaging assessment of viability after chronic infarction in rat hearts. Eur Heart J. 2004; 25:147.
101. Horn M, Weidensteiner C, Scheffer H, et al. Detection of myocardial viability based on measurement of sodium content: A Na-23-NMR study. Magnet Reson Med. 2001; 45(5):756–64.

102. Jerecic R, Bock M, Nielles-Vallespin S, Wacker C, Bauer W, Schad LR. ECG-gated Na-23-MRI of the human heart using a 3D-radial projection technique with ultra-short echo times. Magn Reson Mater Phy. 2004; 16(6):297–302.
103. Parrish TB, Fieno DS, Fitzgerald SW, Judd RM. Theoretical basis for sodium and potassium MRI of the human heart at 1.5 T. Magnet Reson Med. 1997; 38(4):653–61.
104. Ouwerkerk R, Weiss RG, Bottomley PA. Measuring human cardiac tissue sodium concentrations using surface coils, adiabatic excitation, and twisted projection imaging with minimal T-2 losses. J Magn ResonImaging. 2005; 21(5):546–55.
105. Ouwerkerk R, Bottomley PA, Solaiyappan M, et al. Tissue sodium concentration in myocardial infarction in humans: A quantitative Na-23 MR imaging study. Radiology. 2008; 248(1):88–96. [PubMed: 18566171]
106. Pabst T, Sandstede J, Beer M, et al. Optimization of ECG-triggered 3D Na-23 MRI of the human heart. Magnet Reson Med. 2001; 45(1):164–6.
107. Clausen T. Na+-K+ pump regulation and skeletal muscle contractility. Physiol Rev. 2003; 83(4): 1269–324. [PubMed: 14506306]
108. McKenna MJ, Bangsbo J, Renaud JM. Muscle K(+), Na(+), and Cl(+) disturbances and Na(+)-K(+) pump inactivation: implications for fatigue. Journal of Applied Physiology. 2008; 104(1): 288–95. [PubMed: 17962569]
109. Bansal N, Szczepaniak L, Ternullo D, Fleckenstein JL, Malloy CR. Effect of exercise on Na-23 MRI and relaxation characteristics of the human calf muscle. J Magn Reson Imaging. 2000; 11(5):532–8. [PubMed: 10813863]
110. Chang G, Wang L, Schweitzer ME, Regatte RR. 3D 23Na MRI of human skeletal muscle at 7 Tesla: initial experience. Eur Radiol. 2010; 20(8):2039–46. [PubMed: 20309556]
111. Sweeney G, Klip A. Mechanisms and consequences of Na+, K+-pump regulation by insulin and leptin. Cell Mol Biol. 2001; 47(2):363–72. [PubMed: 11355012]
112. Nagel AM, Amarteifio E, Lehmann-Horn F, et al. 3 Tesla sodium inversion recovery magnetic resonance imaging allows for improved visualization of intracellular sodium content changes in muscular channelopathies. Invest Radiol. 2011; 46(12):759–66. [PubMed: 21750464]
113. Amarteifio E, Nagel AM, Weber MA, Jurkat-Rott K, Lehmann-Horn F. Hyperkalemic periodic paralysis and permanent weakness: 3-T MR imaging depicts intracellular 23Na overload--initial results. Radiology. 2012; 264(1):154–63. [PubMed: 22509051]
114. Vilin YY, Ruben PC. Slow inactivation in voltage-gated sodium channels: molecular substrates and contributions to channelopathies. Cell Biochem Biophys. 2001; 35(2):171–90. [PubMed: 11892790]
115. Kushnir T, Knubovets T, Itzchak Y, et al. In vivo 23Na NMR studies of myotonic dystrophy. Magn Reson Med. 1997; 37(2):192–6. [PubMed: 9001142]
116. Constantinides CD, Gillen JS, Boada FE, Pomper MG, Bottomley PA. Human skeletal muscle: Sodium MR imaging and quantification-potential applications in exercise and disease. Radiology. 2000; 216(2):559–68. [PubMed: 10924586]
117. Hofmann WM, Denardo GL. Sodium Flux in Myotonic Muscular Dystrophy. Am J Physiol. 1968; 214(2):330. [PubMed: 5635877]
118. Kopp C, Linz P, Wachsmuth L, et al. Na-23 Magnetic Resonance Imaging of Tissue Sodium. Hypertension. 2012; 59(1):167–72. [PubMed: 22146510]
119. Regatte RR, Akella SV, Borthakur A, Kneeland JB, Reddy R. In vivo proton MR three-dimensional T1rho mapping of human articular cartilage: initial experience. Radiology. 2003; 229(1):269–74. [PubMed: 14519880]
120. Mosher TJ, Dardzinski BJ. Cartilage MRI T2 relaxation time mapping: overview and applications. Seminars Musculoskeletal Radiology. 2004; 8(4):355–68.
121. Ling W, Regatte RR, Navon G, Jerschow A. Assessment of glycosaminoglycan concentration in vivo by chemical exchange-dependent saturation transfer (gagCEST). Proceedings of the National Academy of Sciences. 2008; 105(7):2266–70.
122. Bashir A, Gray ML, Burstein D. Gd-DTPA2- as a measure of cartilage degradation. Magn Reson Med. 1996; 36(5):665–73. [PubMed: 8916016]

123. Filidoro L, Dietrich O, Weber J, et al. High-resolution diffusion tensor imaging of human patellar cartilage: feasibility and preliminary findings. Magn Reson Med. 2005; 53(5):993–8. [PubMed: 15844163]

124. Lesperance LM, Gray ML, Burstein D. Determination of fixed charge density in cartilage using nuclear magnetic resonance. J Orthopaedic Research. 1992; 10(1):1–13.

125. Reddy R, Insko EK, Noyszewski EA, Dandora R, Kneeland JB, Leigh JS. Sodium MRI of human articular cartilage in vivo. Magn Reson Med. 1998; 39(5):697–701. [PubMed: 9581599]

126. Shapiro EM, Borthakur A, Gougoutas A, Reddy R. 23Na MRI accurately measures fixed charge density in articular cartilage. Magn Reson Med. 2002; 47(2):284–91. [PubMed: 11810671]

127. Wheaton AJ, Borthakur A, Shapiro EM, et al. Proteoglycan loss in human knee cartilage: quantitation with sodium MRimaging--feasibility study. Radiology. 2004; 231(3):900–5. [PubMed: 15163825]

128. Reddy R, Insko EK, Leigh JS. Triple quantum sodium imaging of articular cartilage. Magn Reson Med. 1997; 38(2):279–84. [PubMed: 9256109]

129. Rong P, Regatte RR, Jerschow A. Clean demarcation of cartilage tissue 23Na by inversion recovery. J Magn Reson. 2008; 193(2):207–9. [PubMed: 18502158]

130. Trattnig S, Welsch GH, Juras V, et al. Na-23 MR Imaging at 7 T after Knee Matrix-associated Autologous Chondrocyte Transplantation: Preliminary Results. Radiology. 2010; 257(1):175–84. [PubMed: 20713608]

131. Chang G, Madelin G, Sherman OH, et al. Improved assessment of cartilage repair tissue using fluid-suppressed Na-23 inversion recovery MRI at 7 Tesla: preliminary results. Eur Radiol. 2012; 22(6):1341–9. [PubMed: 22350437]

132. Insko EK, Clayton DB, Elliott MA. In vivo sodium MR imaging of the intervertebral disk at 4 T. Acad Radiol. 2002; 9(7):800–4. [PubMed: 12139094]

133. Maril N, Rosen Y, Reynolds GH, Ivanishev A, Ngo L, Lenkinski RE. Sodium MRI of the human kidney at 3 Tesla. Magn Reson Med. 2006; 56(6):1229–34. [PubMed: 17089361]

134. Rosen Y, Lenkinski RE. Sodium MRI of a human transplanted kidney. Acad Radiol. 2009; 16(7): 886–9. [PubMed: 19375951]

135. Hausmann, D.; Konstandin, S.; Zollner, FG., et al. Sodium imaging of the prostate at 3T. Proceedings ISMRM; Melbourne (Australia). 2012. p. 546

136. Jacobs MA, Ouwerkerk R, Kamel I, Bottomley PA, Bluemke DA, Kim HS. Proton, Diffusion-Weighted Imaging, and Sodium (Na-23) MRI of Uterine Leiomyomata after MR-Guided High-Intensity Focused Ultrasound: A Preliminary Study. J Magn ResonImaging. 2009; 29(3):649–56.

137. Wetterling F, Corteville DM, Kalayciyan R, et al. Whole body sodium MRI at 3T using an asymmetric birdcage resonator and short echo time sequence: first images of a male volunteer. Phys Med Biol. 2012; 57(14):4555–67. [PubMed: 22722731]

138. Babsky AM, Zhang H, Hekinatyar SK, Hutchins GD, Bansal N. Monitoring chemotherapeutic response in RIF-1 tumors by single-quantum and triple-quantum-filtered Na-23 MRI, H-1 diffusion-weighted MRI and PET imaging. Magn Reson Imaging. 2007; 25(7):1015–23. [PubMed: 17707164]

139. Schepkin VD, Ross BD, Chenevert TL, et al. Sodium magnetic resonance imaging of chemotherapeutic response in a rat glioma. Magnet Reson Med. 2005; 53(1):85–92.

140. Chenevert TL, Meyer CR, Moffat BA, et al. Diffusion MRI: a new strategy for assessment of cancer therapeutic efficacy. Molecular Imaging. 2002; 1(4):336–43. [PubMed: 12926229]

141. Schepkin VD, Lee KC, Kuszpit K, et al. Proton and sodium MRI assessment of emerging tumor chemotherapeutic resistance. NMR Biomed. 2006; 19(8):1035–42. [PubMed: 16894643]

142. Babsky AM, Zhang H, Hekmatyar SK, Hutchins GD, Bansal N. Monitoring chemotherapeutic response in RIF-1 tumors by single-quantum and triple-quantum-filtered (23)Na MRI, (1)H diffusion-weighted MRI and PET imaging. Magn Reson Imaging. 2007; 25(7):1015–23. [PubMed: 17707164]

143. Schepkin VD, Bejarano FC, Morgan T, Gower-Winter S, Ozambela M, Levenson CW. In vivo magnetic resonance imaging of sodium and diffusion in rat glioma at 21.1 T. Magnet Reson Med. 2012; 67(4):1159–66.

144. Madelin G, Jerschow A, Regatte RR. Sodium relaxation times in the knee joint in vivo at 7T. NMR Biomed. 2012; 25(4):530–7. [PubMed: 21853493]

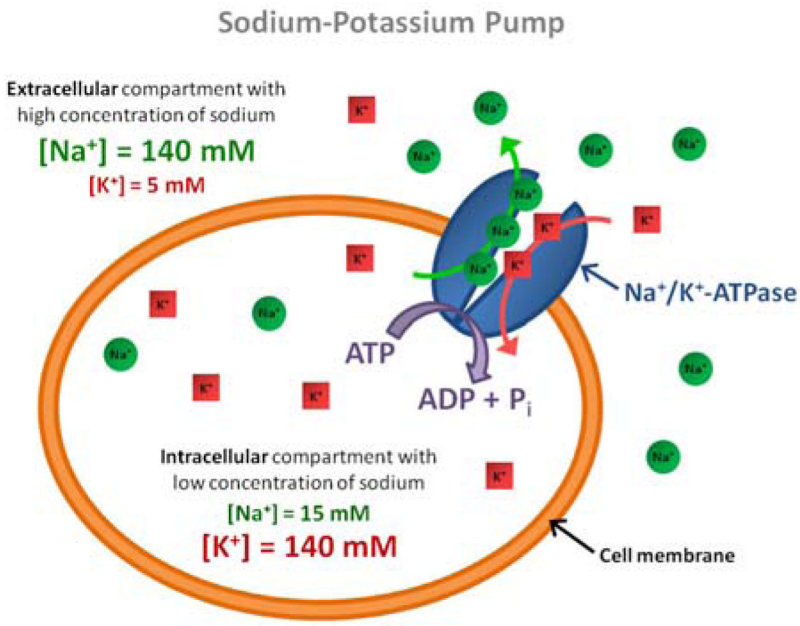

Figure 1.
Schematics of the sodium-potassium pump (Na^+/K^+-ATPase).

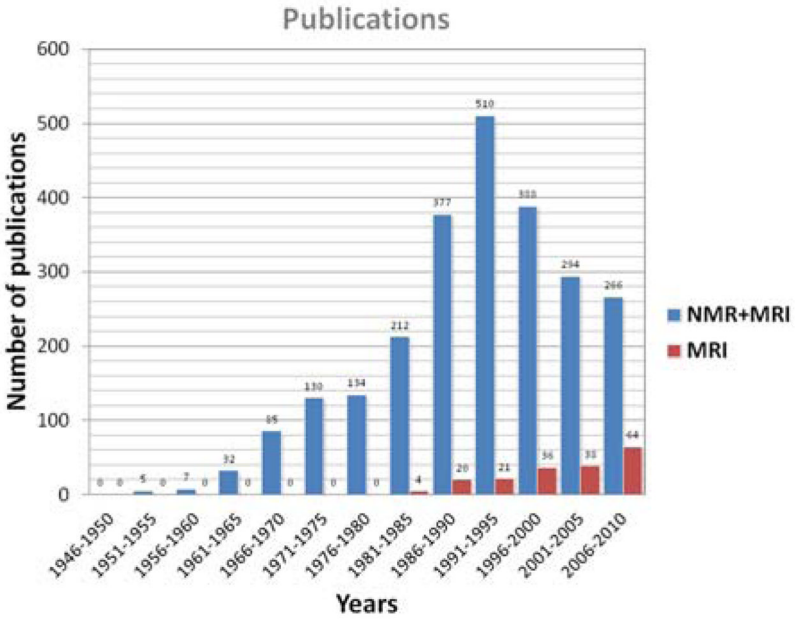

Figure 2.

Publication statistics on sodium NMR and MRI. Data was obtained from a research in Google Scholar with the research key words “sodium” or “23Na” along with “magnetic resonance” or “magnetic resonance imaging” or “MRI” or “NMR” in the publication title.

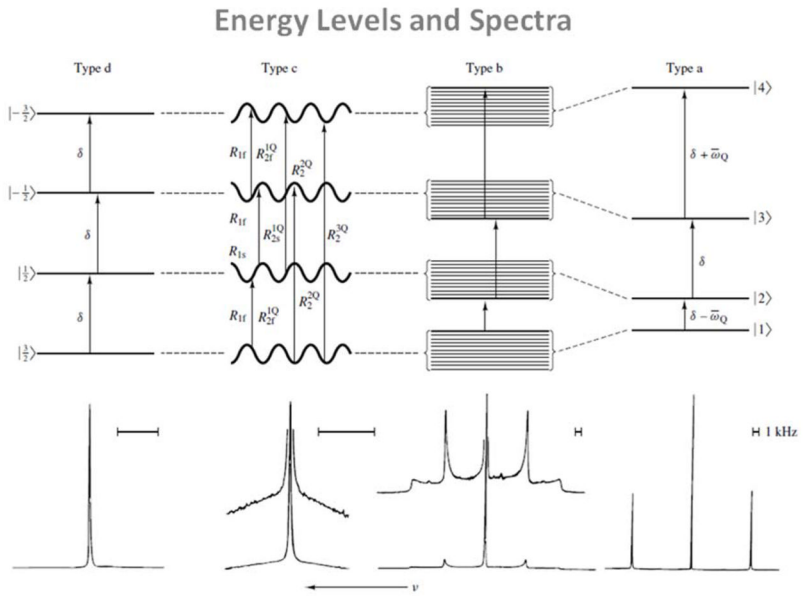

Figure 3.

Typical energy levels and corresponding NMR spectra of sodium nuclei in different environments. Four types of motionally narrowed SQ spectra are possible (a, b, c, and d). The **type-a** (crystal-like) and **type-b** (powder-like) spectra are of Na^+ in aqueous suspensions of oriented and unoriented dodecyl sulfate micelles, respectively. The **type-c** (homogeneous, biexponential, super-lorentzian-like) spectrum is that of Na^+ in an aqueous solution that has a high concentration of micelle-solubilized gramicidin channels. The **type-d** (liquid-like) spectrum is that of NaCl in H_2O. From Rooney W. et al. NMR Biomed 4, 209–226, 1991. Reproduced by permission of Wiley-Blackwell.

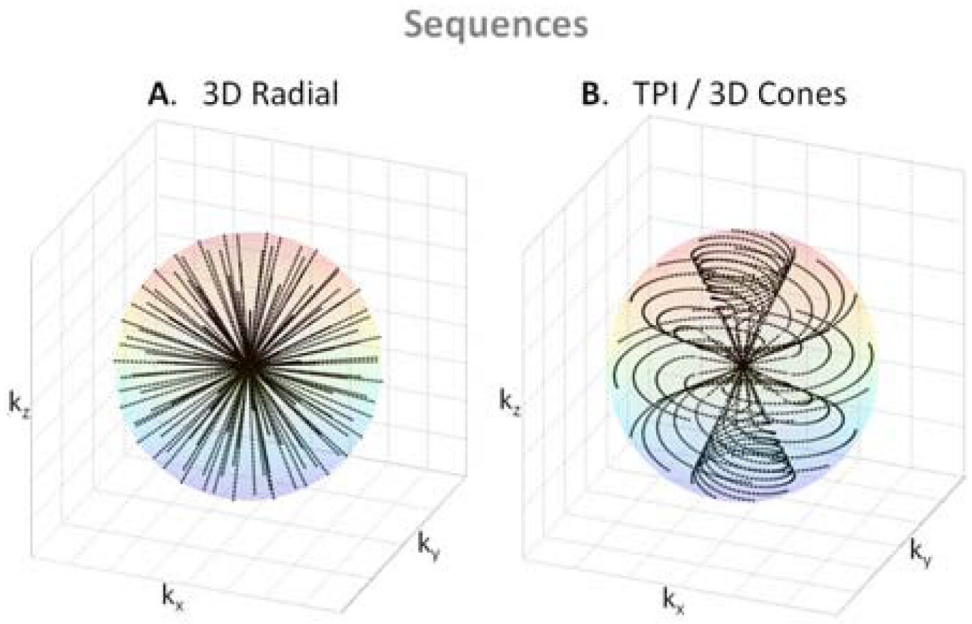

Figure 4.
K-space trajectories from 2 UTE sequences. **A**: 3D radial. **B**: Twisted projection imaging (TPI) or 3D cones types of sequences.

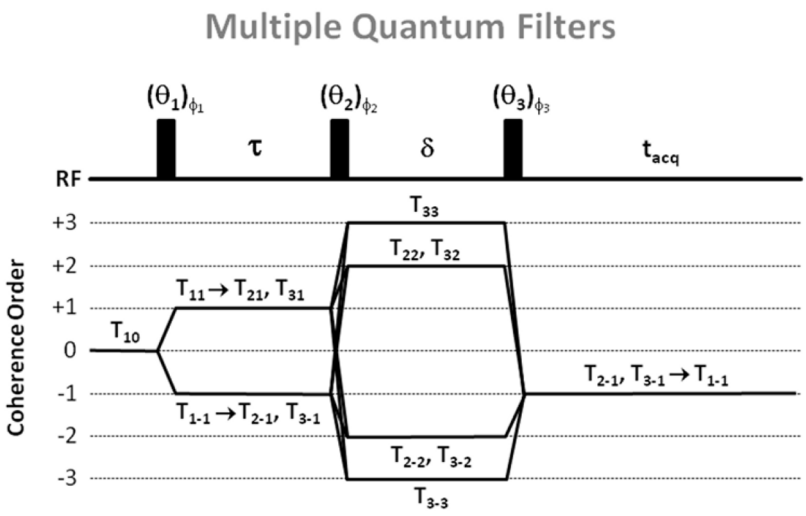

Figure 5.

Multiple quantum filters (MQF) and coherence order transfers. For triple quantum filter (TQF) with six-phase cycling, $\theta_1 = \theta_2 = \theta_3 = 90°$, $\varphi_1 = 30°, 90°, 150°, 210°, 270°$ and $300°$, $\varphi_2 = \varphi_1 + 90°$, $\varphi_3 = 0°$. For double quantum filter (DQF) with four-phase cycling, $\theta_1 = \theta_2 = \theta_3 = 90°$, $\varphi_1 = 0°, 90°, 180°$, and $270°$, $\varphi_2 = \varphi_1$, $\varphi_3 = 0°$. For DQF with magic angle (DQF-MA), $\theta_1 = 90°$, $\theta_2 = \theta_3 = 54.7°$, and the phase cycling is the same as for DQF. For all filters, the receiver phase alternates between 0° and 180°.

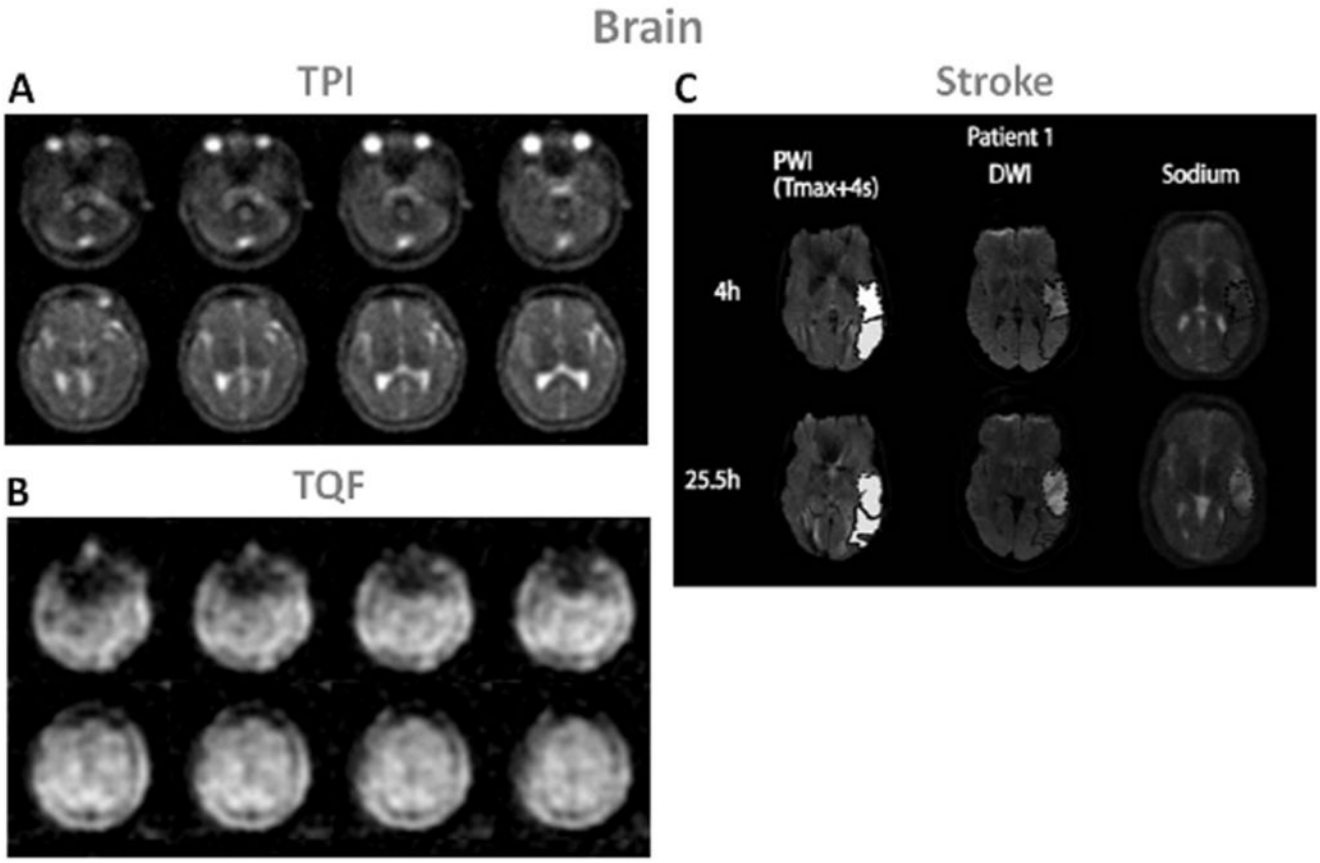

Figure 6.

Examples of brain images. **A**: Twisted projection imaging (TPI) at 3T of a healthy brain. **B**: Triple-quantum filtered (TQF)-TPI at 3T of a healthy brain. **C**: Representative perfusion weighted imaging (PWI), diffusion weighted imaging (DWI) at 1.5T and sodium TPI at 4.7T of the brain of a patient with acute ischemic stroke. These images show the hypoperfused (Tmax+4s) perfusion maps, the DWI hyperintense (core) in dotted outline and the PWI-DWI mismatch tissue (penumbra) in solid outline, and corresponding sodium images, acquired 4h and 25.5h after symptom onset. Figures A and B: Courtesy of Professor F. Boada, New York University Medical Center / University of Pittsburgh Medical Center. Figure C from Tsang A. et al. J Magn Reson Imaging 33:41–47, 2011. Reproduced by permission of Wiley-Blackwell.

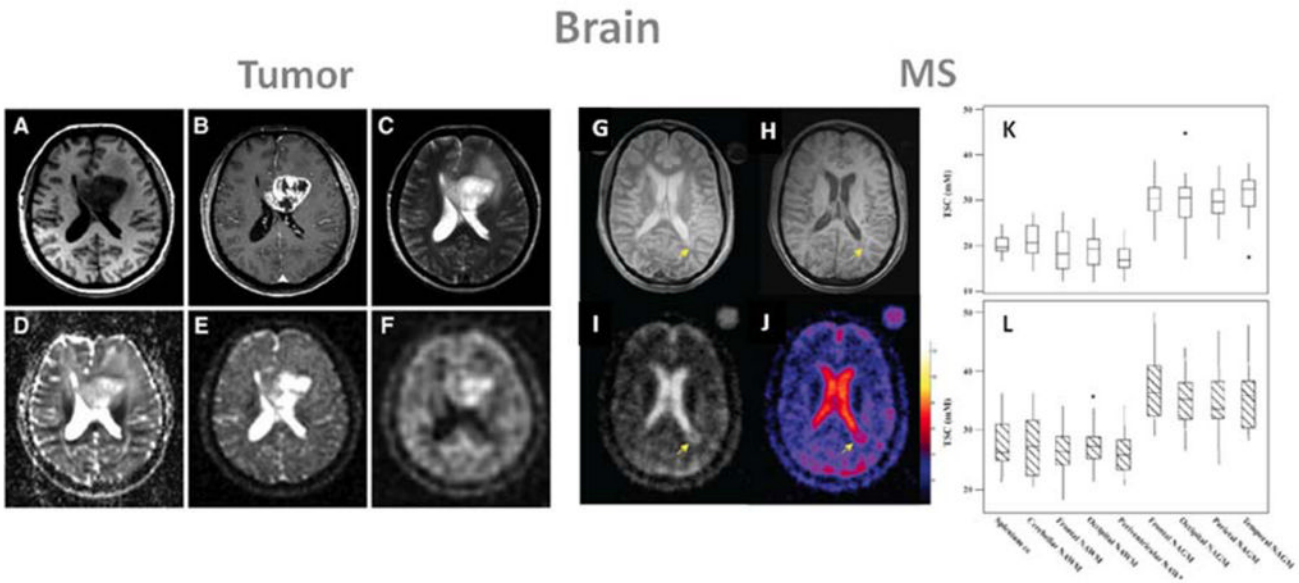

Figure 7.

Examples of brain images: A–F form a patient with glioblastoma (WHO grade IV) of the left medial frontal lobe., and G–L: images and tissue sodium concentrations (TSC) from a patient with multiple sclerosis (MS). **A**: T1 weighted MRI, **B**: T1 weighted MRI with contrast medium (rim enhancement), **C**: T2 weighted MRI showing cystic and solid portions of the lesion and perifocal brain edema, **D**: DWI showing elevated ADC values in the center of the tumor, **E**: sodium MRI showing increased sodium signal in the tumor, **F**: sodium MRI with fluid suppression by inversion recovery (IR), also showing increased sodium signal mainly at the center of the tumor. Proton images (A–D) were acquired at 3T while sodium images (E, F) were acquired at 7T. **G**: proton density MRI, **H**: T1 weighted MRI, **I**: sodium MRI, **J**: corresponding TSC map. **K**: box-plot of the mean TSC value distribution in regions of white matter and grey matter in healthy controls. **L**: box-plot of the mean TSC value distribution in regions of the corresponding normal appearing white matter (NAWM) and normal appearing grey matter (NAGM) in patients with relapsing-remitting MS. cc is corpus callosum. Figures A–F from Nagel A. et al. Investigative Radiology 46(9), 539–547, 2011. Reproduced by permission of Wolters Kluwer Health. Figures G–L from Inglese M. et al. Brain 133, 847–857, 2010. Reproduced by permission of Oxford University Press.

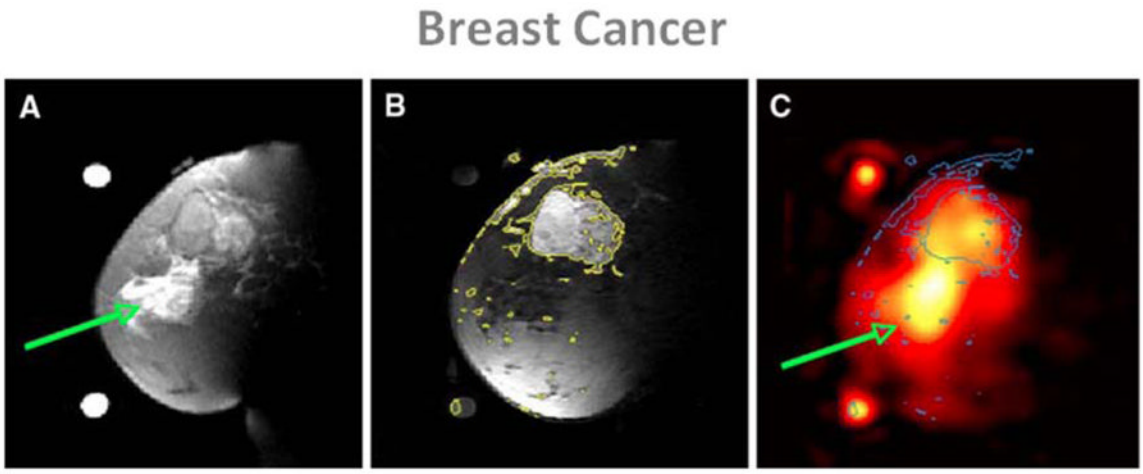

Figure 8.
Examples of breast cancer images from a patient with 5.5 cm infiltrating poorly differentiated ductal carcinoma (T3) at the 12 o'clock position in the left breast. **A**: Fat suppressed T2 weighted MRI showing a mass with T2 intermediate signal and edematous T2 bright retroareolar glandular tissue (arrow). **B**: Fat suppressed t1 weighted MRI post-Gd injection with contour levels in yellow, showing enhancement of the mass at 12 o'clock but not in the retroareolar glandular tissue. **C**: Sodium MRI with contours from B superimposed in blue. Region with edema is indicated by the green arrow. From Ouwerkerk R. et al. Breast Cancer Res Treat DOI 10.1007/s10549–006–9485–4, 2007. Reproduced by permission of Springer Science and Business Media.

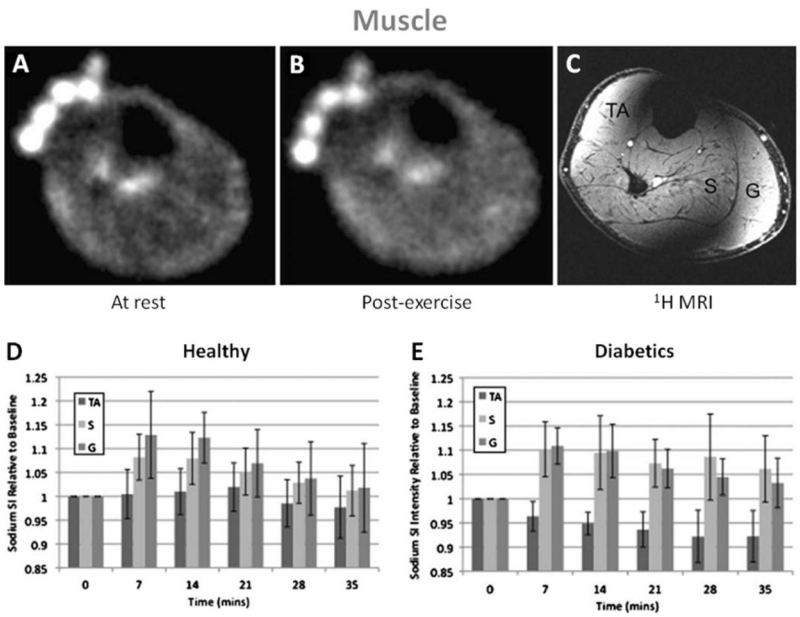

Figure 9.

Example of sodium images in the muscle at rest (**A**) and post-exercise (**B**). 3D FLASH proton MRI (**C**) was performed after the sodium MRI to delineate muscle anatomy: TA is tibialis anterior, S is soleus and G is gastrocnemius. In healthy subjects (**D**), sodium signal intensity increases significantly in S and G just after exercice, but not in the control muscle TA. The sodium intensity then decreases to near baseline in both S and G with a half-time of around 22 min. In diabetics subjects (**D**), sodium signal intensity increases significantly in S and G just after exercice, but not in the control muscle TA. The sodium intensity then decreases to near baseline half-times of around 37 min in S and 27 min in G. From Chang G. et al. European Radiology, DOI 10.1007/s00330–010–1761–3, 2010. Reproduced by permission of Springer Science and Business Media.

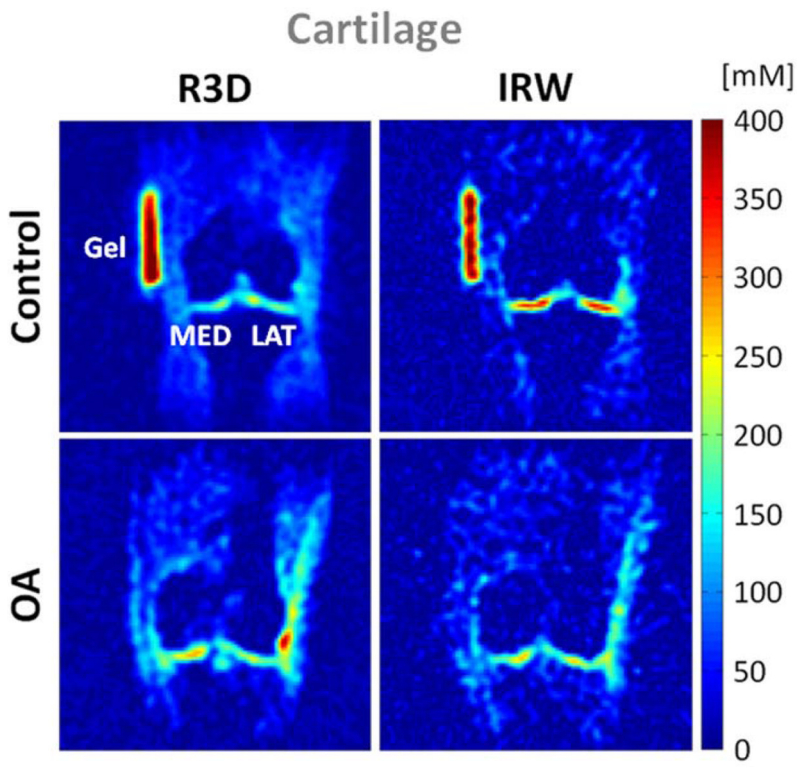

Figure 10.
Example of cartilage sodium concentration maps from a healthy volunteer (control) and a patient with osteoarthritis (OA). Images were acquired with 3D radial (R3D) and IR WURST (IRW). IR WURST was used to suppress fluids through inversion recovery (IR) with an adiabatic WURST pulse in order to increase the sensitivity of the method to change of sodium concentration within the cartilage only. MED = femoro-tibial medial and LAT = femoro-tibial lateral cartilage.

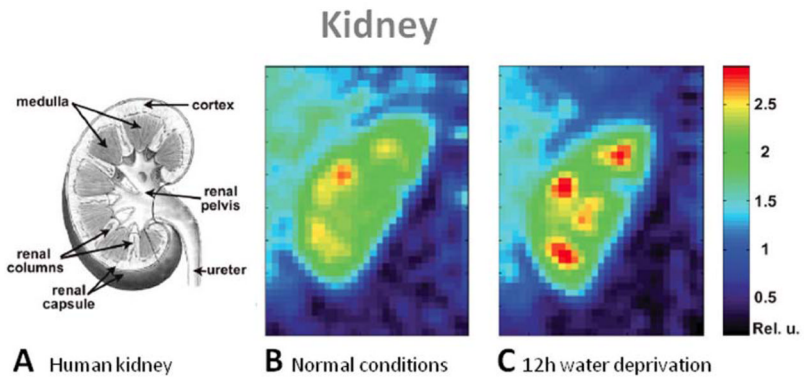

Figure 11.

Examples of kidney images. **A**: Scheme of a human kidney. Central coronal slices of the 3D sodium images of a human kidney under normal conditions (**B**) and 12-h water deprivation (**C**). The sodium gradient increases significantly by 25% after water deprivation. From Maril N. et al. Magn Reson Med 56, 1229–1234, 2006. Reproduced by permission of Wiley-Blackwell.

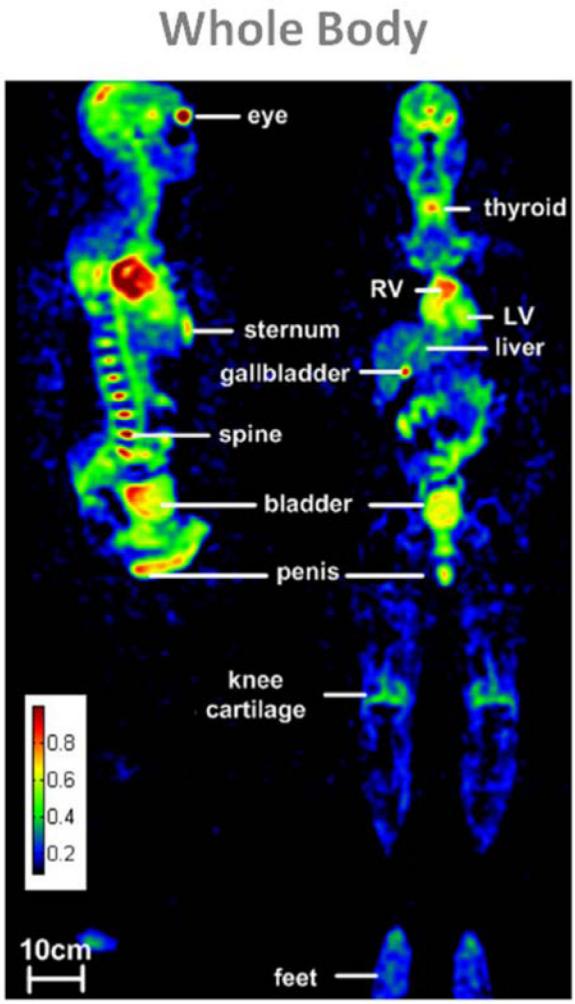

Figure 12.
Example of a whole body sodium image of a male volunteer in sagittal and coronal views. Sodium MRI were acquired at 3T with a 3D radial sequence with density compensation in 5 segments of 10 min each, using an asymmetric birdcage coil. Nominal resolution is 6 mm isotropic. From Wetterling N. et al. Phys. Med. Biol. 57, 4555–4567, 2012. Reproduced by permission of IOP Publishing Ltd.

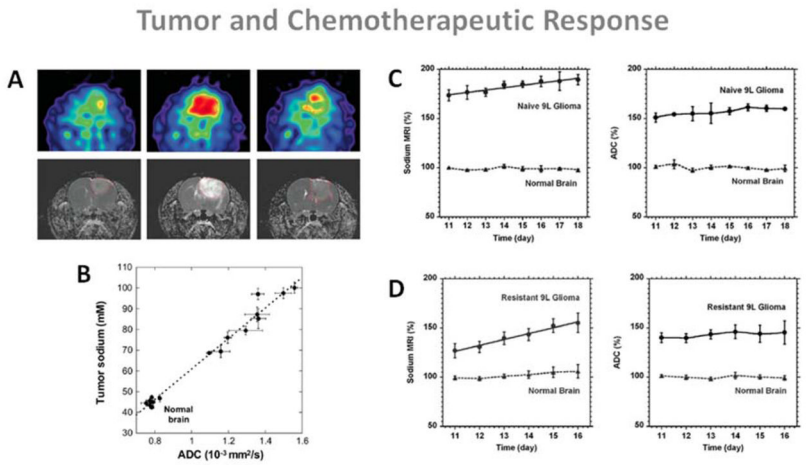

Figure 13.

Examples of sodium MRI and proton DWI studies on tumor and chemotherapeutic response in a rat glioma. **A**: Sodium images (top) and proton ADC maps (bottom) of a BCNU-treated 9L rat glioma acquired at day 0, 7 and 23 (left to right) after BCNU injection, performed at day 17 after tumor implantation. Central sodium image at day 7 show a dramatic increase of sodium concentration throughout the entire tumor area. Image at day 23 shows tumor regrowth after tumor shrinking started at day 9 and its maximum regression at day 16. **B**: Correlation of tumor sodium concentration and ADC in the rat glioma obtained at various points following a single dose of BCNU. **C**: Time course after tumor implantation of sodium (left) and ADC (right) variations for a naive type 9L glioma. Sodium and ADC data are given in percent relative to normal contralateral brain. All data are presented as mean ± standard deviation. Sodium concentration steadily increased in the naive tumor with a rate of 2.4% per day while ADC was practically unchanged (1.4% per day). **D**: Time course after tumor implantation of sodium (left) and ADC (right) variations for a glioma created from a resistant 9L cell line. Sodium concentration steadily increased in the resistant tumor with a rate of 5.8 % per day while ADC was practically unchanged (1.2% per day). Sodium values were corrected for partial volume effect. Figures A and B from Schepkin V.D et al. Magn Reson Med 53:85–92, 2005. Figures C and D from Schepkin V.D. et al. Magn Reson Med 67:1159–1166, 2012. Reproduced by permission of Wiley-Blackwell.

Table 1

Range of sodium concentrations and relaxation times in some human tissues *in vivo.* Values were taken from (24, 68, 71, 85, 109, 112, 116, 126, 144) and references within, and are just given as an indicator of the order of values that we can encounter *in vivo*.

Tissue	$[Na^+]$ (mM)	T1 (ms)	$T2_{short}$ (ms)	$T2_{long}$ (ms)
Brain				
WM	20–60	15–35	0.8–3	15–30
GM	30–70	15–35	0.8–3	15–30
CSF	140–150	50–55	-	55–65
Cartilage	250–350	15–25	0.5–2.5	10–30
Blood	140–150	20–40	2–3	12–20
Muscle	15–30	12–25	1.5–2.5	15–30

Table 2

Irreducible tensor operators for spin I = 3/2. SQC, DQC and TQC are respectively the Single, Double and Triple Quantum Coherences. The anticommutator $[A, B]_+$ for the operators A and B is defined as $[A, B]_+ = AB + BA$.

Tensor Operator	Value	Definition
T_{00}	1	Identity
T_{10}	I_z	Longitudinal magnetization
$T_{1\pm1}$	$\mp\frac{1}{\sqrt{2}}I_\pm$	Rank 1 SQC
T_{20}	$\frac{1}{\sqrt{6}}\left(3I_z^2 - I(I+1)\right)$	Quadrupolar polarization
$T_{2\pm1}$	$\mp\frac{1}{2}\left[I_z, I_\pm\right]_+$	Rank 2 SQC
$T_{2\pm2}$	$\frac{1}{2}I_\pm^2$	Rank 2 DQC
T_{30}	$\frac{1}{\sqrt{10}}\left(5I_z^3 - (3I(I+1)-1)I_z\right)$	Octopolar polarization
$T_{3\pm1}$	$\mp\frac{1}{4}\sqrt{\frac{3}{10}}\left[5I_z^3 - I(I+1) - \frac{1}{2}, I_\pm\right]_+$	Rank 3 SQC
$T_{3\pm2}$	$\frac{\sqrt{3}}{4}\left[I_z, I_\pm^2\right]_+$	Rank 3 DQC
$T_{3\pm3}$	$\mp\frac{1}{2\sqrt{2}}I_\pm^3$	Rank 3 TQC